CHALMERS
UNIVERSITY OF TECHNOLOGY

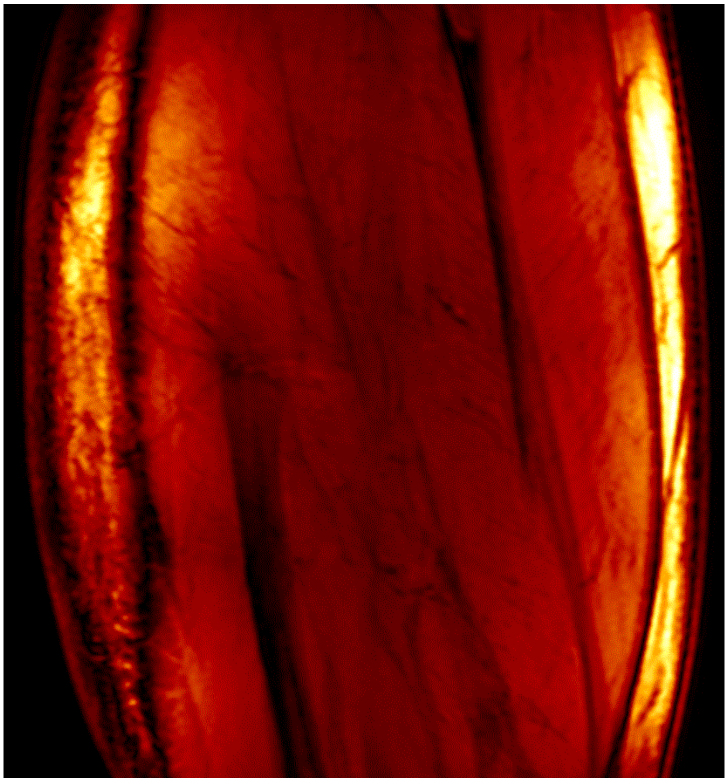

CREATINE CEST IN HUMAN MUSCLE

Master's Thesis in Biomedical Engineering

ESAÚ POBLADOR
RODRÍGUEZ

Department of Signals and
Systems
Chalmers University of
Technology

Gothenburg, Sweden 2015

Master's Thesis 2015: EX068

Master's Thesis in Biomedical Engineering

CREATINE CEST IN HUMAN MUSCLE

ESAÚ POBLADOR RODRÍGUEZ

Department of Signals and Systems
Division of Signal Processing and Biomedical Engineering
CHALMERS UNIVERSITY OF TECHNOLOGY

Gothenburg, Sweden 2015

CREATINE CEST IN HUMAN MUSCLE
ESAÚ POBLADOR RODRÍGUEZ

This work has been performed at the High-Field MR Centre under the supervision of DI Dr. Wolfgang Bogner.

Department of Biomedical Imaging and Image-guided Therapy.
Medical University Vienna.
Austria

Technical report no 2015: EX068
Department of Signals and Systems
Chalmers University of Technology
SE-412 96 Göteborg
Sweden

Telephone + 46 (0)31-772 1000
http://www.chalmers.se

Cover: Magnetic resonance image of a calf muscle measured by the author

Figures: All figures directly included have been kindly allowed by their authors and include source's reference:

- Hanson, Lars G.-*Danish Research Centre for Magnetic Resonance (DRCMR)*
  http://www.drcmr.dk/MR
  http://www.drcmr.dk/Docs/MRI_English_a4.pdf
- James Keeler.-*University of Cambridge, Department of Chemistry*
  http://www-keeler.ch.cam.ac.uk/lectures/Irvine/
- Thomas L. James.-*University of California, Department of Pharmaceutical Chemistry*
  http://www.biophysics.org/education/james.pdf
- William Reusch.- Michigan State *University, Department of Chemistry*
  http://www2.chemistry.msu.edu/faculty/reusch/VirtTxtJml/Spectrpy/nmr/nmr2.htm#nmr11
- Ladislav Valkovič.- High-Field MR Centre; Medical University Vienna
- Martin Gajdošík.- High-Field MR Centre; Medical University Vienna

Gothenburg, Sweden 2015

CREATINE CEST IN HUMAN MUSCLE
Master's Thesis in Biomedical Engineering
ESAÚ POBLADOR RODRÍGUEZ

Department of Signals and Systems
Division of Signal Processing and Biomedical Engineering
Chalmers University of Technology

ABSTRACT

Chemical Exchange Saturation Transfer (CEST) imaging is a relatively recent technique that allows the detection of endogenous and exogenous compounds (protons or molecules) with enhanced sensitivity. Its application to free creatine (Cr) could replace phosphorous MR spectroscopy (^{31}P-MRS) as the gold standard due to its superior sensitivity and spatial resolution. It would then become a powerful tool for the assessment of treatment outcomes and diagnosis of skeletal muscular disorders (muscular dystrophy).

The present thesis is based on a working CEST MR imaging sequence for detection of Glycosaminoglycan (GAG-CEST) in cartilage and a CEST post-processing tool in Matlab for Amide Proton Transfer (APT) and GAG detection. The scope of the present work covers the implementations necessary to apply this method on phantoms for free Cr detection with maximum CEST effect, investigate how CEST contrast is affected by the Radio Frequency (RF) saturation signal as well as by environmental factors, and finally, obtain an optimized MR sequence to achieve maximal contrast image.

For equal metabolite's concentrations, free Cr was found to contribute to the CEST contrast around 80%, whereas the rest 20% came from PCr. In the ranges presented, the contrast was found linearly dependent with both pH and Cr concentration (gain of 0.6% per mMol). Parameters defining the saturation pulses, such as its amplitude, affect the proton's exchange (in this case causing broadening of the CEST peaks). Others like the type of k-space readout, may yield to asymmetric spectra due to insufficient time between saturation periods.

This knowledge is expected to be further applied for detection of dynamic changes of Cr in the human calf muscle during exercise.

Keywords: CEST; creatine; phosphocreatine; chemical exchange; endogenous contrast; muscle.

ACKNOWLEDGEMENTS

This thesis would not have been possible without the help and support from many people at the High-Field MR Centre, Medical University Vienna.

First of all I would like to have a special mention to my supervisor, Wolfgang Bogner, for giving me the opportunity of coming to Vienna, for his expertise and especially for being always available when I needed guidance.

Thank you Martin, Wolfgang and Stephan to give me the opportunity to join scientific journal sessions, seminars and conferences. I have found you always supportive and willing to help when I needed it.

Thank you Marek for your help to understand the MR principles, your guidance regarding spectroscopy and good advices with phantom's design.

I would also like to express my gratitude to Vladimír Mlynárik and Pavol Szomolanyi not only for their contribution providing the base of the current thesis with a working CEST MR imaging sequence for detection of Glycosaminoglycan (GAG-CEST) in cartilage, but also for their always positive attitude and support.

I would also like to thank Dr. Benjamin Schmitt, Siemens Healthcare Australia, for his contribution providing a working Matlab processing tool for APT and GAG-CEST Imaging.

I am very grateful to Ladislav and Marjeta for their help and support with the dynamic exam and guidance using the necessary equipment.

Thank you to all my office colleges and friends, especially to Lenka, Martin Gajdošík, Michal, Bernhard, Pedro, Benedikt, Lukas, Gilbert, Barbara, Olgica and Radka for always being close, sharing with me interesting discussions, good advices, personal experiences and lot of laughs.

I would like to extent my gratitude not only to those directly involved in any way in this thesis but also to the rest of my colleges who have made me feel part of them. Thank you all.

Finally, a special mention to Raquel, for your always wise personal advices and for being part of this adventure that have made me enjoy this period of my life. Thanks for being there.

My gratitude to Oesterreichische Nationalbank (OeNB) for the grant "*Jubläumsfond*" #16133. This thesis has been part of the project "Mapping aberrant myocardial creatine kinase metabolism via frequency labeled exchange transfer" supported by this fund.

NOMENCLATURE

Δ

$\Delta\nu_{1/2}$ - Linewidth at half height 12

1

^{13}C-MRS - Carbon MR Spectroscopy 15
^{1}H-MRS - Proton MR Spectroscopy................ 16

3

^{31}P-MRS - Phosphorous MR spectroscopy..........2

A

A.U. - Arbitrary units 50
ADC - Analog to Digital Converter 21
ADP - Adenosine diphosphate 18
APT - Amide Proton Transfer 2
ATP – Adenosine triphosphate........................2

B

B_0 - Static magnetic field 7
B_1 - Oscillating RF field.................................8
B_1^- - Received RF oscillating field......................8
B_1^+ - Transmitted RF oscillating field 8
B_{eff} - Effective local magnetic field.................. 13

C

C_{A-} Base's concentration............................. 29
CEST - Chemical Exchange Saturation Transfer .1
C_{HA} - Acid's concentration 29
CK - Creatine Kinase....................................2
CMROI - Center for Magnetic Resonance and Optical Imaging 3
Cr - Creatine..2

D

DICOM - Digital Imaging and Communications in Medicine 28
DS - Direct Saturation................................ 26

F

FA - Flip Angle 8
FFT - Fast Fourier Transform...................... 22
FID - Free Induction Decay 8
FLASH - Fast Low Angle Shot Imaging 43
fMRI - Functional MRI.................................1
FOV - Field Of View 33
FT - Fourier Transform.............................. 10

G

GAG - Glycosaminoglycans 2
Glu - Glutamate..2

I

ICE - Siemens reconstruction code environment 28
IDEA - Siemens pulse sequence programming environment in C++................................ 28
IFT - Inverse Fourier Transform 22

K

k_{sw} - Exchange rate 42

L

LG - Lateral Gastrocnemius 32

M

M - Magnetic moment 7
MG - Medial Gastrocnemius 32
MI - Myoinositol 2
MRI - Magnetic Resonance Imaging 1
MRS - Magnetic Resonance Spectroscopy 1
MT - Magnetic Transfer 1

N

NMR - Nuclear Magnetic Resonance 1

O

OeNB - Oesterreichische Nationalbank ii

P

PBS - Phosphate Buffered Saline 29
PCr - Phosphocreatine 2
PD - Proton Density 1
Pi - Inorganic phosphate 17
pK_a - Logarithmic acid dissociation constant 30

R

RF - Radiofrequency 3
ROI - Region of interest 40

S

S_0 - Non-saturated signal 26
SAR - Specific Absorption Rate 45
SNR - Signal-to-Noise Ratio 18
S_{sat} - Saturated signal 26

T

T_1 - Spin-lattice / Longitudinal relaxation time 11
T_2 - Spin-spin / Transversal relaxation time 11
TE - Echo Time 43
TR - Repetition Time 43

V

V_{sample} - Resonance frequency 14

Γ

γ - Gyromagnetic ratio 7

Δ

δ - Chemical shift 14

Ρ

ρ - Spin density 22

Σ

σ - Shielding constant 13

Ω

ω_0 - Angular frequency 7
ω_{RF} - Transmitter angular frequency 8

CONTENTS

1. INTRODUCTION

The traditional Nuclear Magnetic Resonance (NMR) has been extensively used as a non-invasive and non-ionizing method to study living tissues. It was first described by Isidor Rabi in 1938[1], who was awarded with the Nobel Prize in Physics for his discovery of NMR. After him Felix Bloch (Stanford) and Edward Mills Purcell (Harvard) were jointly laureate with such a distinguished award in 1952 "for their development of new methods for nuclear magnetic precision measurements and discoveries in connection therewith".[2]

NMR evolved into two branches which have many features in common: Magnetic Resonance Spectroscopy (MRS), which provides information about the metabolic state and Magnetic Resonance Imaging (MRI), which provides information about the structure and composition in the form of an image.

New generations of NMR techniques have been subsequently developed that combine spatial and chemical information, some examples are:

- **Functional MRI (fMRI):** Detecting signal changes due to neural activity.
- **Diffusion MRI:** Based on the diffusion of water molecules and commonly applied to track nerve fibers (i.e., in Neurological disorders).
- **MR Angiography:** Based on contrast agents or flow effects, are used to highlight arteries for stenosis/aneurysms evaluation.
- **Magnetic Transfer MRI:** This is able of enhancing contrast by indirect measurement of macromolecular contents in tissue.
- **Susceptibility Weighted Imaging:** Based on susceptibility differences between tissues and applied for tumors, vascular and neuro-vascular diagnostics.

The present thesis makes use of a method called chemical exchange saturation transfer (CEST), which is a relatively newly developed contrast mechanism that is similar to the Magnetic Transfer MRI technique. It is based on the magnetization transfer from one population of nuclei (solute population) to bulk water population, in this case by chemical exchange. Magnetic Transfer (MT) can be used as a contrast method, like T1, T2 and PD (Proton Density) since the MR signal decay depends on the exchange rate between bulk water and solute populations. The CEST method will be covered in more detail in Section 2.4.

There are tools available in diagnostic medicine to measure complex molecular changes in vitro like biopsy, body fluids and cultured cells, however for in vivo diagnosis and treatment assessment, Clinical Imaging is used. Optical Imaging has limited applications due to relatively poor depth penetration, Nuclear Medicine has the drawback of using radioactive isotopes and MRS is a successful tool to measure metabolite concentration, though it suffers from low spatial and temporal resolutions. MRI in the other hand is a non-ionizing, non-invasive tool with high spatial resolution, however is nowadays clinically used mostly with exogenous contrast agents for molecular imaging evaluations.

CEST imaging is a relatively recent technique that allows the detection of endogenous and exogenous compounds (protons or molecules) with enhanced sensitivity.[3] Some endogenous metabolites used recently in vivo to generate contrast using this technique and their applications are:[4]

- **Amide Proton Transfer (APT):** Amide protons (-NH) exchange applied for cancer/stroke diagnosis.
- **Glutamate** (Glu)**, Creatine (Cr):** Amine protons (-NH_2) exchange applied for skeletal muscle and myocardial energetics characterization and disorders diagnosis.
- **Glycosaminoglycans (GAG), glycogen, myoinositol (MI), glucose:** Hydroxyl protons (-OH) exchange applied for Osteoarthritis (GAG), neurological disorders (MI) and cancer metabolism studies (glucose).

Creatine Kinase (CK) reaction is the most immediate mechanism to regenerate ATP (adenosine triphosphate), illustrated by the following formula:

$$ADP + PCr + H^+ \overset{CK}{\leftrightarrow} Cr + ATP \qquad (1.1)$$

During muscle contraction the phosphocreatine (PCr), which is a storage of cellular energy, is converted into free creatine (Cr) to maintain ATP, the supply of the energy currency, on a constant level.

Phosphorous MR spectroscopy (^{31}P-MRS) is nowadays the gold standard for dynamic studies on muscle energy metabolism. However, now CEST allows the possibility to measure small amounts of endogenous metabolites, such as Cr, with enhanced sensitivity compared to PCr detection. An additional advantage is that the hardware used for CEST MRI is standard (for ^{1}H nuclei) compared with the one specifically needed for ^{31}P-MRS.

Once the technical limitations are cleared, Cr-CEST could replace ^{31}P-MRS, becoming a powerful tool for assessment of treatment outcomes and diagnosis of muscular disorders, due to its superior spatial resolution and sensitivity.

1.1. Contributions in the field

In 1998 V. Guivel-Scharen et al. from the National Institutes of Health, Maryland, showed that CEST technique was able to generate MRI contrast ***in vitro*** based on the exchange rate of endogenous metabolites (urea) at 4.7 T. [5]

In 2000 Azar P. Dagher et al. from the National Heart Lung and Blood Institute, Maryland, managed to map urea distribution ***in vivo*** at 1.5 T via CEST imaging. [6]

Focusing on Cr CEST imaging, Feliks Kogan and Mohammad Haris et al. from the Center for Magnetic Resonance and Optical Imaging (CMROI), Pennsylvania, managed to:

- 2012: Develop a new method to perform a high resolution Cr CEST imaging without main contribution from PCr at 3T. [7]
- 2013: Provide a technique to perform a dynamic exam to show the distribution of free Cr in skeletal muscle before and after exercise with high spatial resolution at 7T. [8]
- 2013: Characterize the previous technique in human muscle but at 3T. [9]
- 2014: Prove the feasibility, for the first time, of mapping free Cr in myocardium tissue in vitro as well as in vivo at 3T [10]

1.2. Aim of the study

The work covered in the present thesis is based on a working CEST MR imaging sequence for detection of Glycosaminoglycan (GAG-CEST) in cartilage [11].

The aim of the present thesis is to find an optimized MR sequence to detect and map free Creatine (Cr) in phantoms. For this purpose it is necessary to understand how CEST contrast is affected by the radiofrequency (RF) saturation signal independently of other factors such as pH, which as will be shown, need to be isolated.

The knowledge achieved will be further applied for detection of dynamic changes of Cr in human's calf muscle in a similar way as the CMROI group did in 2013.

The scope of the present thesis covers the implementations necessary to:

- Obtain multiple consecutive CEST maps over time by running the available static sequence a number of repetitions for a complete dynamic CEST exam.
- Test the environmental effects and specificity of CEST detection in phantom experiments
- Optimize the sequence parameters to reach Cr CEST detection with high image contrast
- Perform a comparison study with 1H-MRS and 31P-MRS

2. THEORY OF NMR

This chapter provides a brief review of the physics behind the branches of NMR that will be mentioned in the present thesis, its principles and how the images/spectra are generated.

The theory covered here is intended to be the essentials to allow the reader with no prior knowledge on NMR to follow this thesis without the need of any additional source of information. Those readers who are already familiar with the basis of NMR, MR Spectroscopy, MR Imaging and CEST Imaging may choose to continue with further chapters, since this one does not contain specific required information. For those interested in a deeper review on any of the subsections, please follow the corresponding references.

2.1. Basis of NMR

For a rigorous treatment of NMR, the quantum mechanics branch of physics would be the most suitable. It provides a description of NMR theory which takes into consideration the quantized nature of radiation and the discrete levels of energy possible of atoms and molecules. However, Classical physics will be applied when possible, to describe the practical aspects of NMR, like the orientation of nucleus spins and how they are affected by RF pulses. [12]

2.1.1. Classical description of NMR

Certain atomic nuclei have a rotation motion around its own axis known as "spin", like ^1H or ^{31}P. The spin of charged protons makes them behave like tiny magnetic bars or dipoles with their axis oriented along the rotation axis. In the absence of an external magnetic field, the directions of these magnetic dipoles are randomly distributed. This is illustrated in *Fig. 2-1*.

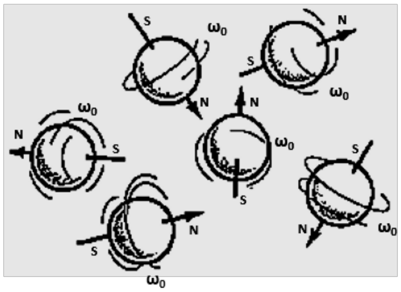

Fig. 2-1: Spin of charged protons makes them magnetic [13]

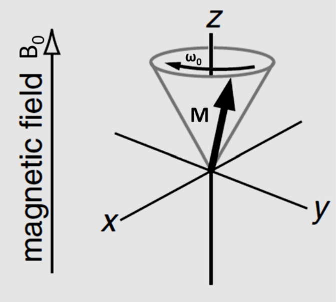

Fig. 2-2: Precession of Magnetization M around B_0[14]

When a magnet is placed in a static magnetic field of a certain direction (commonly represented towards the positive *Z* axis), it aligns along this direction.

However, because the protons have an angular momentum, the magnetic moment "M" will precess with a characteristic angular frequency ω_0, as shown in *Fig. 2-2*.

This is known as the Larmor frequency:

$$\omega_0 = \gamma \cdot B_0 \qquad \text{Eq. 2-1}$$

where B_0 is the applied static magnetic field and "γ" is the gyromagnetic ratio (i.e., a constant that depends on the proton's properties itself). For hydrogen (^{1}H) for instance, $\gamma = 42.58\, MHz/T$.

It is common to express the frequency in Hz. The ***resonance*** frequency at a 7 Tesla scanner would be $v_0 = \gamma \cdot B_0 = 42.58 \cdot 7 = 298.06\, MHz$. Take into consideration that this frequency is in the RF range at which the scanner will transmit pulses required to achieve ***resonance***.[15]

The samples studied contain a large number of protons, so the net effect of all of them is the magnetic moment measured, called "***net magnetization***" or "***bulk magnetization***". In absence of an external magnetic field the spins are randomly oriented, with approximately the same number of spins pointing in all directions, hence the net magnetization is close to zero and do not precess. This is illustrated in *Fig. 2-3*.

After the constant magnetic field B_0 is applied and equilibrium is reached, the added contributions of all magnetic moments results on a net magnetic field along the B_0 direction. This is shown in *Fig. 2-4*.

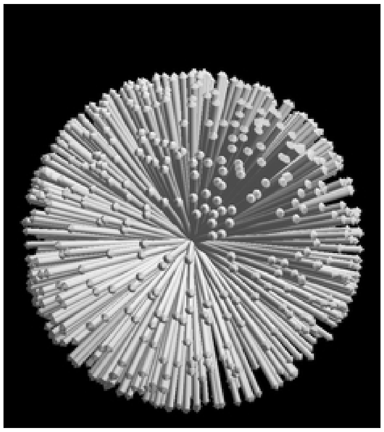

Fig. 2-3: Spins orientation in absence of external B_0 [13]

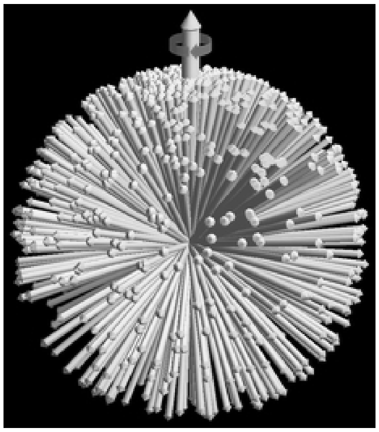

Fig. 2-4: Spins orientation after B_0 is applied [13]

2.1.2. Excitation

In order to detect the precession of the net magnetization vector, a coil is placed aligned in the *X* axis (*Y* axis could be used as well) as illustrated in *Fig. 2-5*. This magnetization will induce a current in the receiver coil, which is subsequently amplified and recorded to form the ***free induction decay*** (FID) signal.

To be able to detect the magnetization vector, it is necessary to tilt it from its equilibrium orientation in B_0 direction (positive *Z* axis). This would be achieved by replacing the magnetic field with one applied in the transversal *XY* plane, for example along the *X* axis, rotating then the magnetization vector to precess towards the *XY* plane, as shown in *Fig. 2-6*.

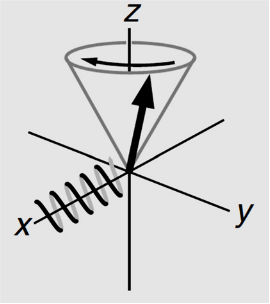

Fig. 2-5: Coil around X axis to detect magnetization [14]

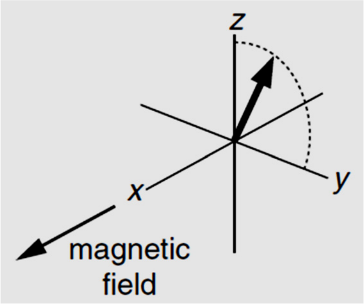

Fig. 2-6: Magnetization rotation towards transverse plane [14]

Unfortunately, the magnetic field cannot be switched on and off so suddenly. Instead, an ***RF excitation pulse*** (B_1) is applied, which is able to tilt the magnetization away from the *Z* axis even in presence of the static magnetic field B_0.

The angle to which the net magnetization vector is rotated relative to the *Z* axis is known as ***flip angle*** (FA). From the equilibrium state it is given by the product of the angular frequency with the time that B_1 is being applied:

$$\mathrm{FA} = \gamma \cdot B_1 \cdot t_p$$

Eq. 2-2

This oscillating RF field (B_1) goes back and forth from +*X* to –*X* axis at a certain frequency ω_{RF}, called ***transmitter angular frequency***. Instead of thinking on B_1 as a linearly oscillating field, one can also divide it into two counter rotating fields $B_1^+$and B_1^- with same amplitude (B_1) and frequency. As they rotate in opposite directions, the fields cancel each other except along the x direction, as illustrated in *Fig. 2-7*.

Starting both fields B_1^+ and B_1^- along the *X* axis, the net field starts being $2 \times B_1$ along the positive *X* axis. When the vectors approach an angle of 90º both fields cancel each other giving a zero net field, and $2 \times B_1$ along the negative *X* axis when vectors reach an angle of 180º. Hence by summing these two fields a linearly oscillating one is produced.[14]

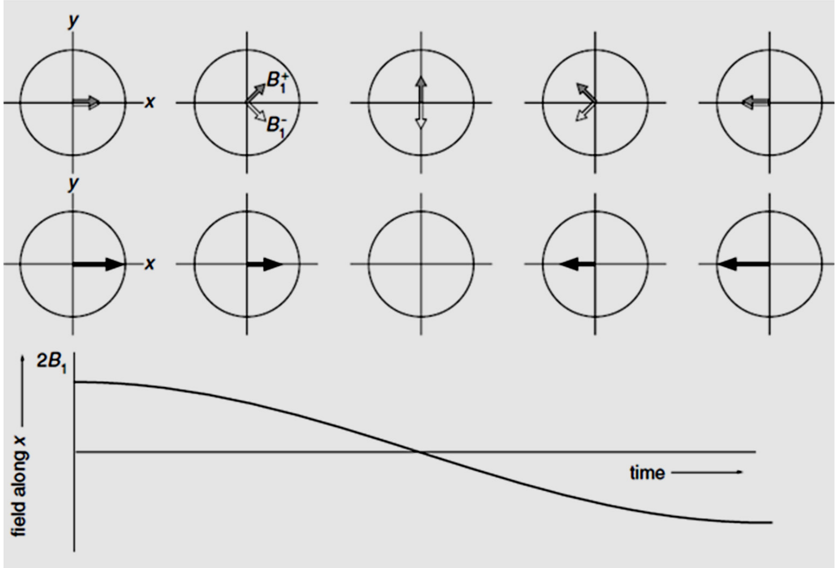

Fig. 2-7: B_1^+ and B_1^- counter-rotating fields (top row). Net B_1, oscillating along the X axis (middle row). Evolution of the field along x with time, amplitude = 2xB_1. [14]

To understand how this weak RF pulses are able to rotate the magnetization, let's introduce the concept of ***rotating frame*** of reference:

If a rotating system is considered, relative to the sample and the NMR scanner, with angular frequency ω_r, the charged protons would precess with angular frequency ω_0 -ω_r. For $\omega_r = \omega_0 = \omega_{RF}$, the nuclei do not appear to precess at all, and consequently considering Eq. 2-1, the apparent static magnetic field B_0 would be zero as well.

The fixed frame of reference is defined with coordinates *x*, *y* and *z*, whereas the labels for the rotating frame are *x'*, *y'* and *z'* (where *z* = *z'*). In the rotating frame, B_1^+ is the only apparent one applied to the nuclei, and because the pulses appear to be static when applied along the *X'* axis, the nuclear magnetization experiences a torque that makes it precess around the B_1^+ direction (*X'* axis) with angular frequency:[12]

$$\omega_{\mathrm{RF}} = \gamma \cdot B_1^+ \qquad \text{Eq. 2-3}$$

Fig. 2-8 shows how for a nucleus with a positive gyromagnetic ratio "γ" and a negative Larmor frequency "-ω_{RF}" (so that the precession goes from +*X* to –*Y* axis), the magnetization coincide with the B_1^- field.

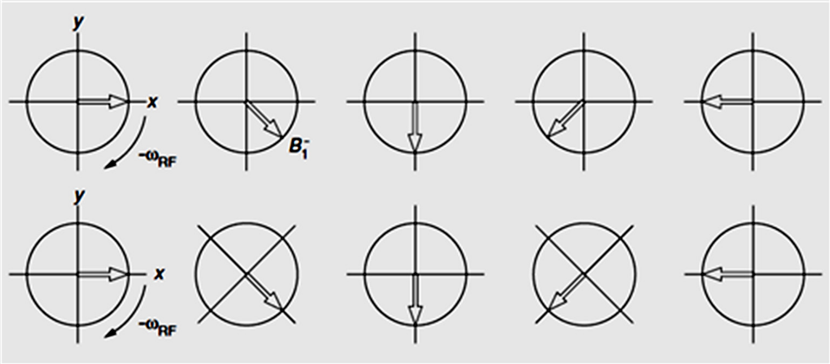

Fig. 2-8: Field rotating at –ω_{RF} viewed in fixed frame of reference (top row). Same field viewed in the rotating frame, appears being static (bottom row). [14]

Therefore, changing the frame of reference, so that it rotates at the same rate as B_1^- ($-\omega_{RF}$), is a mathematical trick which allows to ignore $B_1^+$and consider B_1^- to be static from now on. For a frame of reference rotating at $+\omega_{RF}$, B_1^- would be ignored and B_1^+ would be considered. [14]

From now on B_1^+ will be used for transmitted RF field and B_1^- for the received RF signal. The term B_1 refers to both.

A 90º RF excitation pulse (B_1^+) would rotate the net nuclear magnetization "M_0" towards the transversal *X'Y'* plane (and *XY* plane). At this point, the nuclear spin populations in the Z direction are equalized and the magnetization vector "M_{xy}" is only affected by the static magnetic field B_0, precessing around the *Z=Z'* axis at the Larmor frequency. The *X* and *Y* components of M_{xy} are given by the following expressions when the orientation of M_{xy} is along the positive *X* axis for *t* = 0:

$$M_x = M_0 \cos(\omega_0 t) \qquad \text{Eq. 2-4}$$

$$M_y = M_0 \sin(\omega_0 t) \qquad \text{Eq. 2-5}$$

Their plots are shown in *Fig. 2-9*. The Fourier transform (FT) of them would show a spectrum with a single peak at the Larmor frequency ω_0.

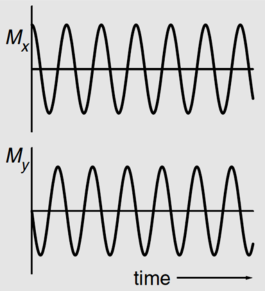

Fig. 2-9: Mx and My components of the magnetization predicted for t=0. [14]

2.1.3. Relaxation

After the net magnetization is taken away from the *Z* axis (i.e. by the application of a 90º RF pulse) it returns to its initial thermal equilibrium by a process called ***relaxation***. Remember that in thermal equilibrium the magnetization vector was oriented towards the direction of the static magnetic field B_0 and was completely coherent ($M_z=M_0$ and $M_{xy}=0$).

This evolution is characterized mainly by two constants:[12]

- T_1, "spin-lattice" or "longitudinal" relaxation time
- T_2, "spin-spin" or "transversal" relaxation time.

T_1 is the time constant to recover the longitudinal magnetization along the B_0 static field direction (i.e. the *Z* axis). The following simplification from the Bloch equation can be used to describe longitudinal relaxation:

$$\frac{dM_z}{dt} = \frac{M_0 - M_z}{T_1} \qquad \textit{Eq. 2-6}$$

$$M_z(t) = M_0\left(1 - e^{\frac{-t}{T_1}}\right) \qquad \textit{Eq. 2-7}$$

T_1 (time needed so that the signal recovers to $1-e^{-1}$ =63% of its initial value) can be measured by the "inversion recovery experiment", illustrated in *Fig. 2-10*. Here the net magnetization recovers to thermal equilibrium after a 180º RF pulse have been applied:

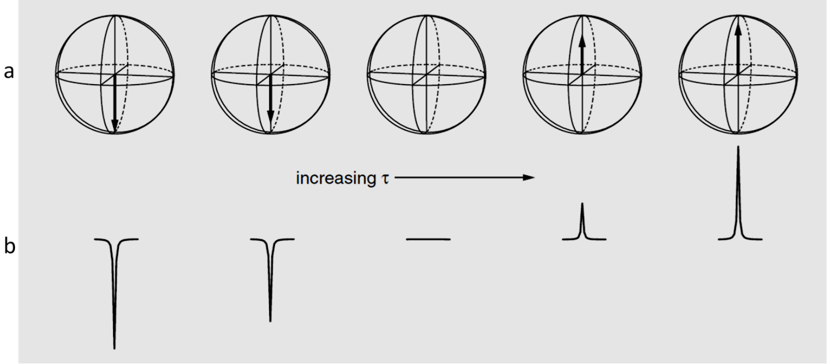

Fig. 2-10: Mz evolution after a 180º RF pulse (inversion recovery experiment) Net magnetization (a) and size and sign of Mz spectra (b). [14]

T_2, on the other hand, is the time constant to decay in the transversal plane (i.e. the *XY* plane). The return to equilibrium follows an exponential decay, hence it can be written as:

$$\frac{dM_{xy}}{dt} = \frac{-M_{xy}}{T_2} \qquad \textit{Eq. 2-8}$$

Fig. 2-11 describes how nuclear spins and net magnetization evolve in the transversal rotating frame *X'Y'* plane after a 90º RF pulse was applied. If there would be a single resonance frequency ω_0, the magnetization would remain constant in the rotating frame of reference. However as ilustrated in ***Fig. 2-11.a***, the spins slightly disperse from the theoretical resonance frequency, this can be explained by the interactions between neighbouring nuclear spins. As the spreading of this range of frequencies "$\Delta\omega_0$"continues, the net magnetization M_{xy} decays since phase coherence is lost as showed in ***Fig. 2-11.b***.

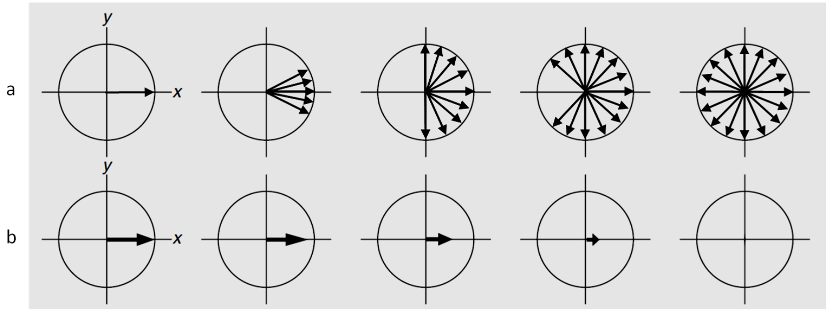

Fig. 2-11: M_{xy} spreading around ω_0, in the rotating frame, after a 90º RF pulse
Individual spins dephasing (a) and net magnetization (b)
Modified from [14]

The relation between T_2, $\Delta\omega_0$ and the resonance linewidth "$\Delta v_{1/2}$" is given by:

$$\frac{1}{T_2} = \frac{\Delta\omega_0}{2} = \pi \times \Delta v_{1/2} \quad \text{Eq. 2-9}$$

The decay of the free precession signal in the transversal plane (M_{xy}) is in reality accelerated by the B_0 field inhomogeneity. Hence M_{xy} decays exponentially with a another time constant $T_2^* < T_2$, so the expression of its components should hence be rewritten as: [12]

$$M_x = M_0\, cos(\omega_0 t) \cdot e^{-t/T_2^*} \quad \text{Eq. 2-10}$$

$$M_y = M_0\, sin(\omega_0 t) \cdot e^{-t/T_2^*} \quad \text{Eq. 2-11}$$

The FID signal is hence produced by one of these decaying waveforms with time (depending on which axis the receiver coil is oriented along), as M_{xy} induces a current in the receiver coil.

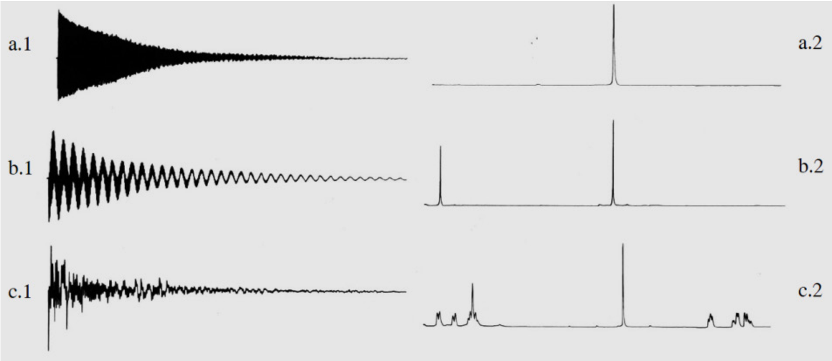

Fig. 2-12: FID signals (left) and its Fourier Transform or Spectrum (Right). [16]

2.1.4. The chemical shift

Nuclei from different elements have different gyromagnetic ratios "γ", hence from Eq. 2-1 one can deduced that their signals will have different frequency at a certain magnetic field B_0 . In a similar way when the local field (B_{eff}) at a nucleus position is slightly different to other nuclei of the same element, it will achieve resonance at a shifted frequency. This is known as ***chemical shift*** and it is expressed in terms of dimensionaless units of parts per million [ppm].

This change in the local magnetic field is caused because the static magnetic field B_0 induces currents in the atom and molecule's electron clouds. These currents, in turn, produce an additional field at the nucleus, proportional and opposite to the applied field (typically a million times smaller).

Therefore the effective local magnetic field at the nucleus can be given by:

$$B_{eff} = B_0 - B_{0\sigma} = B_0(1 - \sigma) \qquad \textit{Eq. 2-12}$$

where σ is called the ***shielding*** constant, because its effect is to shield the nuclei from the applied field and it reflects the chemical environment of the nuclei. This phenomenon is illustrated in ***Fig. 2-13***:

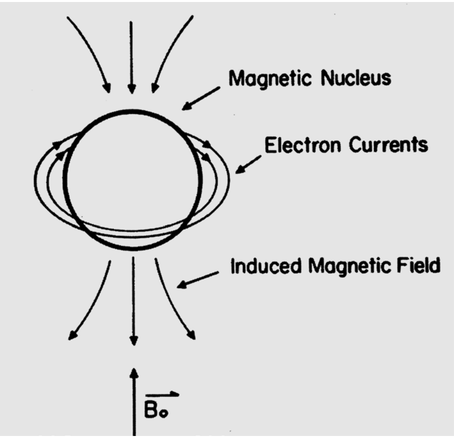

Fig. 2-13: Electron currents induced by B0 and the smaller field opposed to B0 which is yielded [16]

From Eq. 2-12 it is clear that the chemical shift is dependent on the applied static magnetic field. In order to make it independent it is generally expressed in terms of the dimensionless unit of parts per million [ppm]. The chemical shift **δ** is hence defined as:

$$\delta = \frac{\nu_{\text{sample}} - \nu_{\text{Reference}}}{\nu_{\text{Reference}}} \times 10^6 \qquad \textit{Eq. 2-13}$$

V_{sample} is the resonance frequency of the sample in [Hz] and $V_{\text{reference}}$ is an arbitrarily chosen reference frequency. From Eq. 2-12 and Eq. 2-13 $\boldsymbol{\delta}$ can be also expressed as:

$$\delta = \frac{\sigma_{Reference} - \sigma_{sample}}{1 - \sigma_{Reference}} \times 10^6 \qquad \textit{Eq. 2-14}$$

and due to $\sigma \ll 1$, the chemical shift can be simply approximated by the difference between the shielding constants of the reference and the nuclei of interest:[12]

$$\delta = \left(\sigma_{Reference} - \sigma_{sample}\right) \times 10^6 \qquad \textit{Eq. 2-15}$$

2.2. MR Spectroscopy

MRS exploits the fact that chemical shift shows the field variations due to specific chemical environments; therefore its main purpose is to distinguish metabolite signals. MRI on the other hand exploits the chemical shift to provide spatial information. The obtained signal represents a sum of all resonance frequencies.

The principle of “in vivo” MR Spectroscopy is to study a high resolution spectrum of a specific volume within a tissue or organ. These spectra may differ due to metabolism, disease or treatment changes; hence MRS can provide biochemical information.

High resolution NMR gives very good results when the sample is homogeneous, pure and small to fit in a radiofrequency coil. However, when the biomolecules are very large, with complex spectra or mixed with many other substances, the study of a certain organ in vivo may be challenging. [17]

The most common nuclei studied in MRS are hydrogen (^{1}H), phosphorous (^{31}P), carbon-13 (^{13}C) and Sodium (^{23}Na), although the first was ^{1}H, due to its high content in water and fat in tissue.

^{1}H-MRS is able to detect a number of compounds like neurotransmitters, ^{31}P-MRS is widely used to investigate metabolites involved in energetic processes as well as for intracellular pH and ^{13}C-MRS allow studying important metabolic pathways in vivo in a non-invasive way. [18]

2.2.1. Fourier-Transform in MRS

The signal recorded in response to an RF pulse appears as an oscillation which decays with time. In order to obtain an MR spectrum, in which the signal amplitude is expressed as a function of frequency, it is necessary to apply a Fourier transformation.

A sinusoidal signal (infinite in time) would have a single frequency component with no width. However, because in reality there is a distribution of spins oscillating at slightly different frequencies around ω_0, it can be deduced from Eq. 2-9 that the T_2^* relaxation causes a broadening of the resonance line widths.

The resolution of the spectrum is determined by how slowly a signal decays in time domain, hence how narrow it is in the frequency domain. The definition of the spectrum, on the other hand, makes reference to the discrete frequency steps in the signal acquisition and display.

When the signal acquisition is truncated before the FID has completely decayed, its Fourier transformation is convoluted with a sinc function $\left(\frac{\sin x}{x}\right)$, introducing a distortion in form of oscillations. This is minimized in practice by applying a spectral filter (i.e., multiplying the tail of the cut signal in time domain with a small factor), however at the expense of a slight broadening in the frequency peaks. [17] However, usually this situation is avoided by sampling for a sufficiently long period, until the signal has decayed and only noise is sampled at the end of the ADC readout.

When there is more than one resonance frequency, as shown in *Fig. 2-12.b* and especially in *Fig. 2-12.c*, the Fourier transformation makes their discrimination easier to be analyzed in frequency domain.

When it is desirable that all nuclei are exited simultaneously in a frequency range Δv, the duration of the B_1^+ pulse can be approximated by Eq. 2-16. Therefore, in NMR RF pulses are applied as short pulses with enough energy to tilt the magnetization by a desired flip angle (FA) during this short time. [12]

$$t \approx \frac{1}{\Delta v} \qquad \textit{Eq. 2-16}$$

The response to this excitation pulse will show different frequency components when there are nuclei surrounded by different chemical environments.

2.2.2. Proton MR Spectroscopy (^1H-MRS)

The hydrogen nucleus (proton) is the most sensitive, besides tritium, and the most common in nature as shown in *Table 2-1*: [12]

Isotope	Natural Abundance %	Spin (I)	Magnetic Moment (M) [1]	Gyromagnetic ratio (γ) [2]	Gyromagnetic ratio (γ) [3]	Relative sensitivity at constant field [4]
^{1}H	99,98	1/2	2,793	267,530	42,576	100,00
^{2}H	0,02	1	0,857	41,070	6,536	1.5×10^{-4}
^{13}C	1,11	1/2	0,702	67,280	10,705	1.8×10^{-2}
^{17}O	0,04	5/2	-1,893	-36,280	-5,772	--
^{19}F	100,00	1/2	2,627	251,790	40,052	83.0
^{23}Na	100,00	3/2	2,863	70,808	11,262	9.3
^{31}P	100,00	1/2	1,131	108,400	17,235	6.6

Table 2-1: Properties of nuclei commonly used in biology. (Adapted from [12, 19])

[1] *M in units of Nuclear magnetons [Nμ]*

[2] *γ in units of [10^6 rad s^{-1} T^{-1}]*

[3] *γ in units of [MHz T^{-1}]*

[4] *Relative to that of an equal number of protons [12]*

MRI exploits primarily the strong signals arising from protons present in water and lipids; MRS on the other hand detects signals from other metabolites. This is why in ^{1}H-MRS it is generally required to suppress the much larger contributions of water and lipids.

Another difficulty, in particular for in vivo ^{1}H-MRS, is the fact that a large number of metabolites resonate in a relatively narrow chemical shift range. To have sufficiently good separation of these different chemical compounds, narrow signal peaks are anticipated (spectral resolution). This requires an excellent B_0 field homogeneity. From Eq. 2-12 it is derived that the best spectral resolution is achieved when a higher static B_0 field is applied by the scanner, especially for relatively small voxels.

The general distribution of chemical shifts ranges with different functional groups that are characteristic for ^{1}H-MRS are given in *Fig. 2-14*:

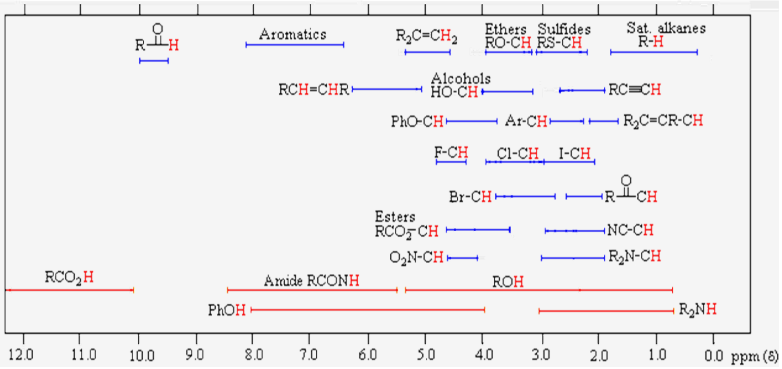

Fig. 2-14: ^{1}H Chemical Shift (δ) ranges relative to TMS (Tetramethylsilane) [20]

2.2.3. Phosphorus MR Spectroscopy (^{31}P-MRS)

Phosphorous nuclei are still the most extensively used for metabolic studies. Compared to ^{1}H-MRS it is less sensitive but features a larger chemical shift dispersion (around 30 ppm for phosphates as illustrated in *Fig. 2-15*), which simplifies quantification.

One of the advantages is that it does not need the suppression of solvent's signals. The most dominant signals in ^{31}P-MRS are originating from those compounds involved in muscle oxidative energetics:

- ATP (α, β and γ)
- Phosphocreatine (PCr)
- Inorganic phosphate (Pi)

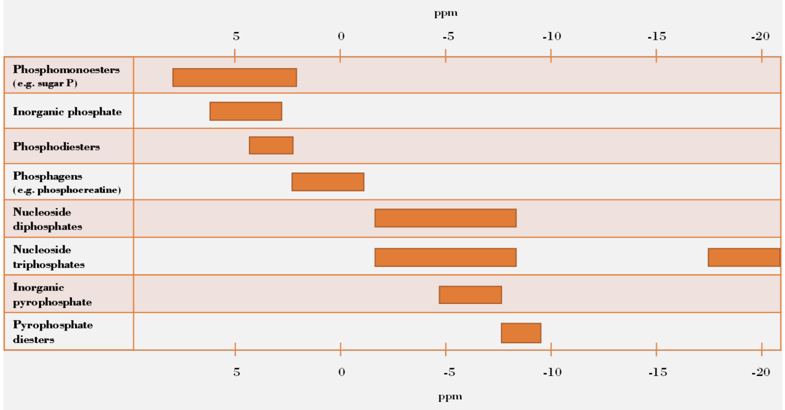

Fig. 2-15: 31P Chemical Shift (δ) ranges relative to PCr (Phosphocreatine) Adapted from [12]

The transition between resting and exercise states in skeletal muscle involves a regulatory process to maintain ATP according to energy demand. The Creatine-kinase (CK) equilibrium previously stated with following expression:

$$ADP + PCr + H^{+} \overset{CK}{\leftrightarrows} Cr + ATP \qquad (1.1)$$

During muscle contraction the phosphocreatine (PCr), which is a storage of cellular energy, is converted into free Cr to replenish ATP, the supply of the energy currency, to keep ATP on an approximately constant level.

Adenosine diphosphate (ADP) signal overlaps with the strongest ATP signal, but ADP is of low concentration, which translates into a low signal-to-noise ratio (SNR). However, ^{31}P-MRS can be used to measure the kinetics of this reaction by indirectly calculating the concentration of free ADP from the measurement of the rest of the reactants and known biophysics assumptions.[12]

2.3. MR Imaging

The NMR theory covered above should enable to understand the principles of MR spectroscopy. In order to obtain an image in magnetic resonance imaging (MRI) the resonance frequency can be also used to encode spatial information.

2.3.1. Spatial Fourier-Transform in MRI

The previous explanations about Fourier transformation in MRS would apply here for 1D (one dimension) imaging. In practice a 2D Fourier transformation is used to generate a sectional image, but the scanner has to be equipped with extra magnets called "***gradient coils***" which are able to cause linear B_0 ***field gradients***, which are required to select or spatially encode a desired volume.

The field experienced by a nuclei located at any position would be given by the Larmor equation affected by the additional gradient field in the following way:

$$\mathrm{B_{eff}} = \mathrm{B_0} + \mathrm{G_r} \cdot \mathrm{r} \qquad \textit{Eq. 2-17}$$

where G_r is the gradient vector and r is the position vector. The resonance frequency of the same compound, hence, varies in the direction of the applied field gradient. In the *X* direction for example, the resonance frequency expression would be:

$$\omega_{eff}(x) = \gamma \cdot (\mathrm{B_0} + G_x \cdot \mathrm{x}) \qquad \textit{Eq. 2-18}$$

Spatial localization may be achieved making use of gradient coils first by ***slice selection and afterwards by phase encoding*** and ***frequency encoding*** of this slice. A standard pulse sequence for a "2D FT" method, as the one depicted in ***Fig. 2-16***, would follow these tree stages:

- "Slice selection": Transmitting a frequency selective RF pulse while a slice gradient "G_{Slice}" is applied
- "Phase encoding": Apply a gradient "G_{Phase}" between excitation and readout to encode the position in one direction within the already selected slice
- "Frequency encoding": Use a readout gradient "$G_{Frequency}$" during signal readout to encode the position in the perpendicular direction

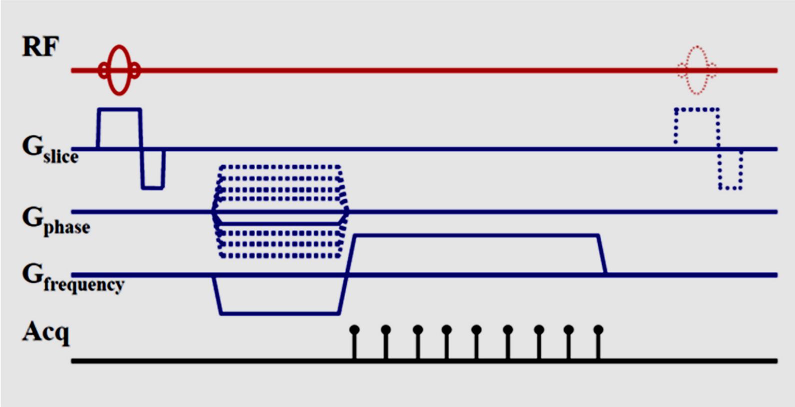

Fig. 2-16: Example of RF pulse and gradient timings for a 2D FT image sequence

2.3.2. Slice selection

If a frequency-selected RF pulse is transmitted while a field gradient is being applied, the resonance condition will be accomplished in a plane perpendicular to the gradient, as is illustrated in *Fig. 2-17*:

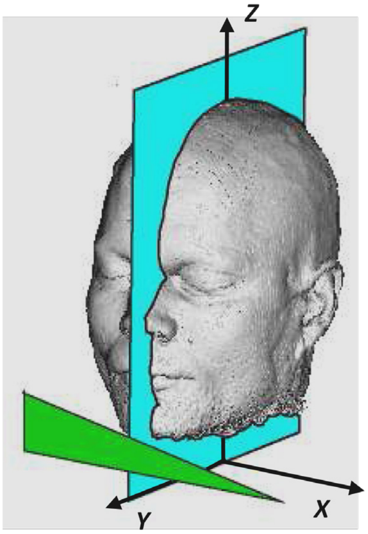

Fig. 2-17: Spins are influenced selectively (Sagittal slice) when a gradient is applied (from left to right) while RF pulse is transmitted. Modified from [13]

For coherence with *Fig. 2-17*, the convention to follow from now on is that the gradients applied are "G_X" for slice selection, "G_Y" for reading and "G_Z" for phase-encoding. So for a gradient applied in the *X* direction, the thickness of the slice "Δx" would be determined by the magnitude of the field gradient "G_X" and the frequency bandwidth of the RF pulse:

$$\Delta x = \frac{\Delta\omega}{\gamma \cdot G_x}$$

Eq. 2-19

It is desirable that the intensity profile across the thickness of the slice is as uniform as possible, while falling off steeply outside of the slice. This ideal profile corresponds to a step or rectangle shape in frequency domain and infinitely long sinc function in the time domain.

The usual way to select the RF pulse is a truncated modified sinc function so that its duration in time is reasonably short. Its profile after Fourier transformation is similar to a trapezoidal central shape with some residual oscillations at both sides.

There is an undesirable effect when an RF pulse is transmitted while a gradient field is applied, there is a distribution of different spins phases across the thickness of the slice. To counteract the loss of net signal produced, a negative gradient is applied to ***refocus*** the spins to recover the same phase between them, see *Fig. 2-16*.

2.3.3. Phase encoding

After the slice is set, the next step would be to encode one of the spatial directions within the slice to measure the nuclei distribution along this dimension. Applying the same logic as in Eq. 2-18, the nuclei aligned along the *Y* direction (same position along the *Z* axis), would have the same resonance frequency:

$$\omega_{eff}(z) = \gamma \cdot (\mathrm{B}_0 + G_z \cdot \mathrm{z}) \qquad \text{Eq. 2-20}$$

Nevertheless the frequency offset caused by the gradient G_z to those along the *Z* direction is given by:

$$\Delta\omega = \gamma \cdot G_z \cdot z \qquad \text{Eq. 2-21}$$

As a result of this variation, after a certain time ***t***, there will be a phase shift of:

$$\Delta\phi = \gamma \cdot G_z \cdot z \cdot t \qquad \text{Eq. 2-22}$$

The rate at which the nuclei accumulate a phase shift, for a given value in this direction, depends on the amplitude and duration of the gradient at a certain *Z* position. Hence there are two ways to perform the scan, vary the time duration at a fix gradient strength or what is shown in *Fig. 2-16*, a constant duration with incrementally increased gradient amplitudes "G_{Phase}".

This phase shifts remain after the G_{Phase} is applied, so that it can be used to encode the location in this direction prior the signal readout.

2.3.4. Frequency encoding

The next step to follow is the localization of nuclei distribution along the *Y* axis. Different positions in this direction will have different frequencies if a gradient in this direction "G_Y" is applied during acquisition of the NMR response. This is known as frequency encoding.[17]

Finally the spin density is spatially located making use of k-space encoding.

2.3.5. The concept of k-space and image generation

The raw data acquired during the readout is stored in a 2D grid called "***k-space***", "***Fourier space***" or "***reciprocal space***". In the most extent method called "spin-warp", the axis labels k_x and k_y represent the frequency gradient amplitude in the "read" direction and the gradient amplitude for a fixed phase encoding interval, respectively.

The sampling of k_x is typically performed during one ADC (Analog to Digital Converter) readout, while k_y is acquired following consecutive excitation steps with incrementally increasing phase-encoding gradient amplitudes. Each point in k-space corresponds to a spatial harmonic in the image space.

Let's describe what is happening at a certain moment in the protocol described above, after the gradient fields have been applied while the last sampling for a certain trajectory in the ***k-space*** is taking place (illustrated in *Fig. 2-18* by the vertical red line):

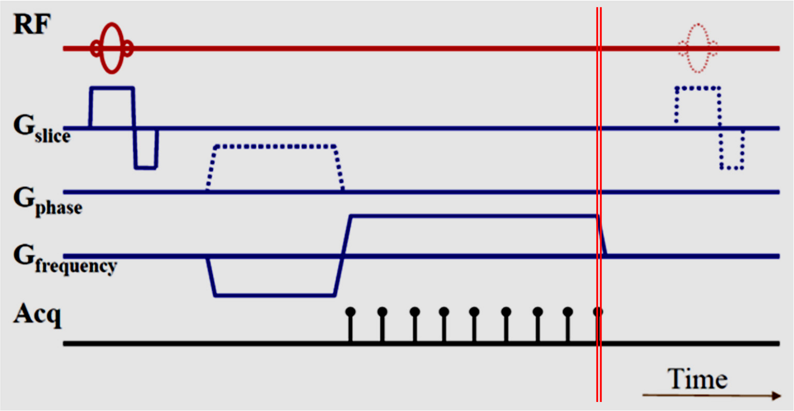

Fig. 2-18: Sampling the last point of a trajectory in the 2D k-space

The illustration on the left side of *Fig. 2-19* shows the spin patterns of a homogeneous distribution of protons within a slice, at the moment stated in *Fig. 2-18*, after the RF pulse has been transmitted and the gradient fields have been applied.

For each spin pattern, a vector ***k*** is assigned (right side of *Fig. 2-19*), the orientation of which shows the direction of the pattern's maximum gradient and its length represents the density of the stripes. After an inverse 2D Fourier transform (2D IFT) of this single point is performed, depicted in the middle of *Fig. 2-19*, a grid structure in spatial domain is created for this relatively high spatial frequency in the k_x direction and a relatively high spatial phase in the k_y direction.

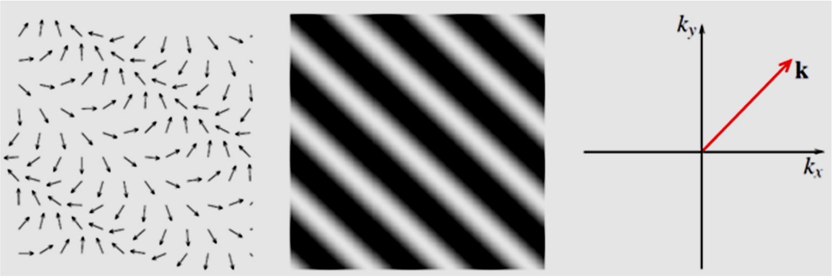

Fig. 2-19: Sampling the last point of a trajectory in the 2D k-space

To reconstruct the full image, a number of points in k-space is sampled, the patterns of which are added up and weighted by the MR-signal measured. The mathematical tool to do it is applying a 2D FFT [15]

This is possible because the information, in this case the spin density "$\rho(r)$" has been encoded properly so that the signal $S(t)$ depends on the spin density and phase at a certain position (remember that the resonance frequency is constant for all spins).

For simplification let's consider an example in one dimension where the signal is coming from two spots at positions $-x_0$ and x_0. A gradient G_x is applied along the **X** direction during sampling, so applying Eq. 2-22, the phase of the spot located at x_0 would be:

$$\phi_{G(x_0,t)} = -\gamma \cdot G_x \cdot x \cdot t \qquad \text{Eq. 2-23}$$

and the phase accumulated in position $-x_0$:

$$\phi_{G(-x_0,t)} = \gamma \cdot G_x \cdot x \cdot t \qquad \text{Eq. 2-24}$$

The total signal sampled is hence given by:

$$s(t) = S_0 \cdot e^{-i \cdot \gamma \cdot G_x \cdot x_0 \cdot t} + S_0 \cdot e^{+i \cdot \gamma \cdot G_x \cdot x_0 \cdot t} = 2S_0 \cdot cos(\gamma \cdot G_x \cdot x_0 \cdot t) \qquad \text{Eq. 2-25}$$

and applying a change of variable:

$$s(k) = 2S_0 \cdot cos(\mathrm{k} \cdot x_0) \qquad \text{Eq. 2-26}$$

where S_0 is the amplitude in each spatial position. So as stated before, applying the 2D FFT yields to the original spin density:

$$\rho(x) = \frac{1}{2\pi}\int_{\infty}^{+\infty} 2S_0 \cdot cos(\mathrm{k} \cdot x_0) \cdot e^{-i\cdot\mathrm{k}\cdot x}\, dk$$

$$= \frac{S_0}{2\pi}\int_{-\infty}^{+\infty} e^{i\cdot\mathrm{k}\cdot(x+x_0)} + e^{i\cdot\mathrm{k}\cdot(x-x_0)} dk$$

$$= S_0\big(\delta(z+z_0) + \delta(z-z_0)\big) \qquad \textit{Eq. 2-27}$$

which represent two peaks with amplitude S_0 at positions $-x_0$ and x_0, as expected.

Fig. 2-20 shows how patterns can be added to form a typical brain image and how some single points in the k-space contribute to the image by looking at their 2D-IFT:

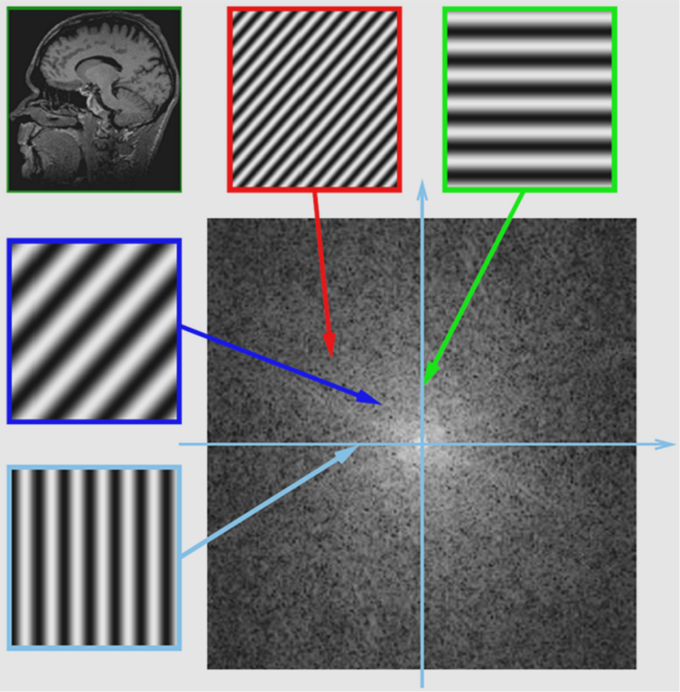

Fig. 2-20: Structure of k-space as a function of the k vector.[13]

It is clear how the coded information in k-space has a brighter region in the middle (where the low frequencies are located), showing that there are more constant and low frequency components contributing to the image. In other words, the slow varying patterns will have higher weight coefficients when they are added up.

2.4. CEST Imaging

It has been explained in 2.1.4 how the chemical environment by which the nucleus is surrounded affects its resonance frequency resulting in a chemical shift (**δ**). ***C***hemical ***E***xchange makes reference to a process in which the nuclei in aqueous condition can move from one environment to another at a certain rate, which controls the equilibrium of this process.

This mechanism is illustrated in *Fig. 2-21* and *Fig. 2-22(a)*, where the measured free H_2O resonance signal is generated by protons spending part of the time in solution (blue protons) and part time bound (green protons) to molecules such as amides (-NH), amines ($-NH_2$), hydroxyl (-OH), membranes or other groups.

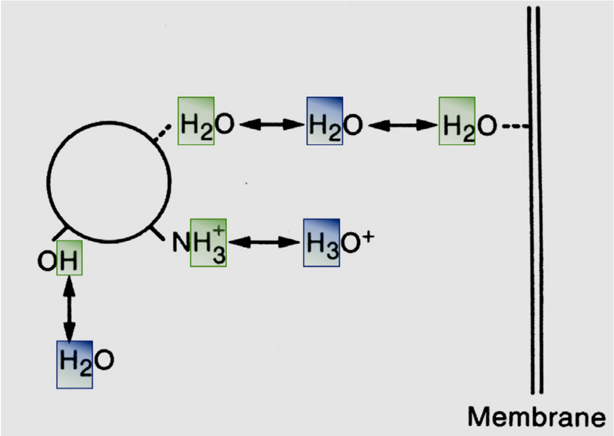

Fig. 2-21: Chemical exchange between free protons (blue) and bounded ones to membranes and molecules (green).[16]

When the exchange rate between two pool sites (A and B) is fast enough, a single peak at the averaged following resonance frequency is detected: [16]

$$\omega = f_A \cdot \omega_A + f_B \cdot \omega_B \qquad \textit{Eq. 2-28}$$

The line widths “$\Delta\omega_{1/2}=\frac{1}{\left(\frac{1}{T_2}\right)}$” are governed by:

$$\frac{1}{T_2} = \frac{1}{T_{2A}} + \frac{1}{T_{2B}} \qquad \frac{1}{T_1} = \frac{1}{T_{1A}} + \frac{1}{T_{1B}} \qquad \textit{Eq. 2-29}$$

being f_A and f_B the ratios at which the nuclei stay at pools A and B, respectively, so that $f_A + f_B = 1$. For a fast exchange regime, the exchange rates have to be much larger than the chemical shift difference $\Delta\omega=\omega_A-\omega_B$. On the other hand a slow exchange regime would produce two separate resonance peaks in the spectrum at the resonance frequencies in sites A and B respectively.

Saturation ***T***ransfer makes reference to an experiment which takes advantage of the fact that magnetization can be transferred. When a population of spins is saturated, its longitudinal net magnetization approaches zero. Thus, bound dissolved labile protons can be labeled by saturation and indirectly detected as a signal decrease from the free protons population in bulk water after exchange of this labeling. This is known as ***C***hemical ***E***xchange ***S***aturation ***T***ransfer (CEST).

When the exchange rate and the saturation time are sufficiently high, the RF radiation at the solute frequency (6.5 ppm for Cr) causes a visible saturation effect at the water resonance frequency, as depicted in *Fig. 2-22(b)*. The reduced net magnetization from the solute pool protons accumulate in the water pool in sufficient quantity, which allows its indirect measurement and imaging of compounds as relatively low-concentrated compounds such as creatine with higher sensitivity.

CEST imaging is possible due to the reduction of water signal. However, in order to detect two separate resonance peaks at water (w) and solute (s) pools, the exchange rate must be in the slow to intermediate regime:[4]

$$k_{sw} \leq \Delta\omega \qquad \text{Eq. 2-30}$$

where k_{sw} represents the exchange rate from the solute pool to the free water pool and $\Delta\omega$ the chemical shift.

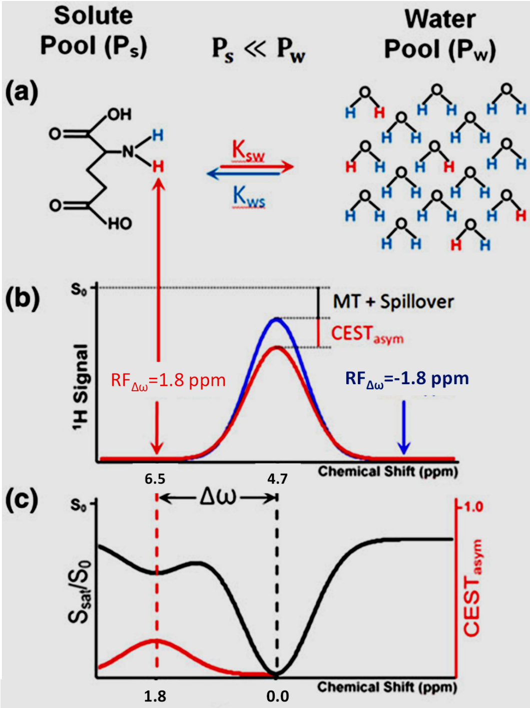

Fig. 2-22: Chemical Exchange Saturation Transfer (CEST): Principles and contrast enhancement mechanism. Modified from [4]

(a) Saturated solute protons "Ps" (red) at 6.5 ppm for Cr's protons in Chemical Exchange with water pool protons "Ps" (blue)

(b) Decrease in H_2O signal due to MT, DS and CEST effects

(c) CEST effect isolated from MT and DS effects through the calculation of Z-spectrum and CEST asymmetry analysis.

In reality the RF saturation pulses are not perfectly frequency selective, hence causing undesired direct saturation (DS) of the water signal, also known as "spillover" effect. Fortunately, the DS spectrum is characterized by a symmetric shape around the H_2O resonance frequency at 4.7 ppm.

There are also other competing mechanism, which decrease the water signal such as the traditional magnetic transfer (MT), which is based on the saturation transfer between semi-solid macromolecules and free bulk water.[21] This MT effect can be detected in a much wider frequency range and contrary to MT-effects the CEST effect is visible much closer to the water frequency (±5ppm).[22] Hence, for high static magnetic fields (B_0) and mobile protons with small chemical shift as Cr (1.8 ppm) MT effects are attenuated and approximately symmetric.

The contrast enhancement for imaging is firstly achieved by calculating the Z-spectrum or CEST-spectrum, in which the spectra of the saturated signal S_{sat} is normalized by the non-saturated signal S_0 (*b*lack curve at *Fig. 2-22(c)*). For the Z-spectrum the water frequency is considered the center frequency and assigned to 0 ppm.

Secondly, the analytical tool to calculate contrast or CEST effect is known as CEST-asymmetry ratio. It performs a subtraction of the water signal from one side of the CEST-spectrum from its mirrored side:

$$CEST_{asym} = \frac{S_{sat}(-\Delta\omega)-S_{sat}(+\Delta\omega)}{S_0} \qquad \text{Eq. 2-31}$$

where the chemical shifts $-\Delta\omega$ and $\Delta\omega$ are considered with respect to water frequency (-1.8 ppm and 1.8ppm away from H_2O resonance frequency, respectively). The result of such an analysis is illustrated as a red curve in *Fig. 2-22(c)*. It can be seen how CEST effect is isolated from MT and DS (spillover) effect because it is the only one being asymmetric relative to the center frequency.

In conclusion this analysis assumes:[3]

- ✓ Independent contributions from water and solute pools due to the slow to intermediate condition.
- ✓ Symmetry of non-CEST contributions around the water signal coming from MT and DS from water protons.
- ✓ Accumulation of saturation in water pool protons has long enough lifetime to detect partial saturation signal at water resonance frequency

3. MATERIALS

The materials needed to carry out the current master thesis are located at the High-Field MR Centre in Vienna and have been provided by the Department of Biomedical Imaging and Image-guided Therapy of the Medical University of Vienna.

MR scans were performed on a 7T MR system (MAGNETOM, Siemens, Erlangen, Germany). The MR Scanner software ($^{®}$Syngo MR Numaris 4, Siemens, Erlangen, Germany) is the registered software provided by *Siemens AG*. *Siemens IDEA* (pulse sequence programming environment in C++) has been used to modify the MR sequences. *Siemens ICE* (reconstruction code environment) images have been used for comparisons with Matlab processed images.

CEST analysis of raw data in DICOM format (Digital Imaging and Communications in Medicine) was based on Matlab software, releaseR2015a (MathWorks, Natick, Massachusetts, USA), with student license for Chalmers students.

MRS quantification of raw data in DICOM format was performed based on jMRUI software (D. Graveron-Demilly group, Université Claude Bernard Lyon 1, France) using the time domain-fitting routine AMARES under academic license.

3.1. Equipment

The MR scanner used is the whole body 7T MR Magnetom system from Siemens Healthcare, Erlangen, Germany shown in *Fig. 3-1*.

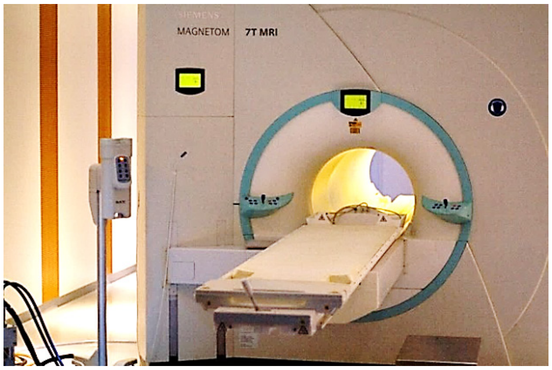

Fig. 3-1: Whole body 7T MR Magnetom Scanner Siemens Healthcare

An air pressure-based pneumatic MR-compatible ergometer (Trispect, Ergospect, Innsbruck, Austria), shown in *(*Fig. 3-2.*a)* and (*Fig. 3-3.a*), was used for the dynamic measurement of CEST in vivo.

The coils used and their applications were:

- ✓ ^{1}H 28-channel Tx/Rx knee coil from QED, Mayfield Village, Ohio, USA, for CEST imaging.(Fig. 3-2.*b)*

- ✓ ^{31}P 10 cm Tx/Rx surface coil for ^{31}P-MRS. (*Fig. 3-3.b*)

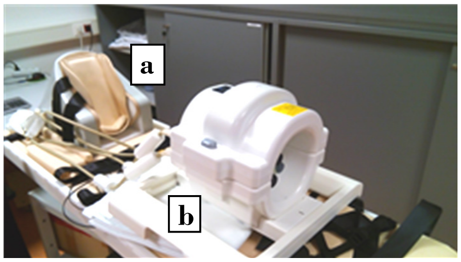

Fig. 3-2. a: Air pressure-based pneumatic ergometer
b: ^{1}H 28-channel knee coil

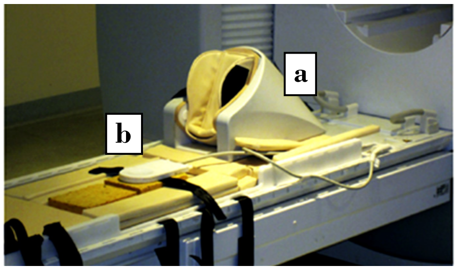

Fig. 3-3. a: Air pressure-based pneumatic ergometer
b: ^{31}P Tx/Rx 10 cm surface coil[23]

3.2. Phantoms

To identify the CEST effect in aqueous condition, solutions have been kept sealed in the syringes shown in Fig. 3-4. In order to maintain the static magnetic field B_0 as homogeneous as possible, they were placed in the center of a cylindrical bottle filled with water. The handmade phantom used is illustrated in Fig. 3-5.

Fig. 3-4. Labeled syringes with sample solutions

Fig. 3-5. Phantom with samples sunken in tap water

In order to control the pH of the samples, the solutions have been prepared in a Phosphate-buffered Saline (PBS) made from two salts:

- Phosphate monobasic (KH_2PO_4), acting as acid.
- Phosphate dibasic (K_2HPO_4), acting as its conjugate base.

The salt's concentration was calculated according to the Henderson-Hasselbalch equation, to have enough total concentration (200 mMol/l) to maintain the pH constant during the period of the study:

$$pH = pK_a + log\left(\frac{C_{A-}}{C_{HA}}\right) \qquad \text{Eq. 3-1}$$

where "C_{HA}" corresponds to the acid*'s concentration* (KH_2PO_4), "C_{A-}" *corresponds to the base's concentration* (K_2HPO_4) *and* pK_a is the *logarithmic acid dissociation constant (6.82 at 25°C)*.

The final adjustment of pH was done using a calibrated HI 98130 pH-meter from Hanna Instruments and by adding small amounts of base/acid salts.

4. METHODS

The purpose of this chapter is to explain how the work was planned and performed. As it has been stated in Chapter 1, the final purpose of the present work is to be able to measure dynamic changes of free Cr in the human calf muscle during exercise. Therefore, the first step was to modify the available static CEST sequence to increase (i) the number of frequencies at which the solute protons were going to be saturated and (ii) the number of repetitions for which a complete CEST exam was acquired to obtain multiple consecutive CEST maps over time.

Because it was not possible to change the image reconstruction on the scanner (ICE program), the next step was to analyze and modify an available off-line Matlab program to process the raw data in a similar way as the ICE Siemens software does it, but providing additional features that could not be implemented in ICE. This program was previously used to process data for different CEST studies on the following metabolites: Amide Proton Transfer (APT) and GAG-CEST Imaging. However, it was not able to process data acquired dynamically, and needed certain modifications to process Cr-CEST images properly.

Complementary implementations were also needed to allow debugging, as well as registering and plotting the results at intermediate steps during the data processing. In other words, one important step was to convert the start-up processing Matlab tool (the output was just a DICOM image) into an improved evaluation tool. This means that the MATLAB program was extended in such a way as to allow the selection of certain voxels or regions of interest (ROI) by the user, to show the voxels/regions being processed at any time, to plot Z-spectra and CEST-asymmetry analysis, and finally to register and export the processed data automatically into Excel tables (for independent regions/samples) in addition to reconstruction of the Cr-CEST maps and exporting into DICOM format.

Preliminary data on dynamic CEST-based Cr measurements were finally acquired, but a careful optimization is still required and many technical challenges remain, which are out of the scope of the current thesis due to its extent. The effort was hence focused on changing both, the MR sequence parameters and the Matlab processing/analysis tool to detect free Cr in phantoms with maximum contrast by achieving maximum CEST effect, which will further help to optimize the techniques for dynamic in vivo measurements.

The different tasks or steps followed have been organized in the flowchart shown in *Fig. 4-1*. The tasks are grouped together depending on their requirements to be programmed or set-up:

- **MR sequence:** Require changes in the sequence programming code using C++

- **Scanning:** Require setting-up certain parameters through the user interface
- **Data processing:** Require changes in the processing tool programming in Matlab

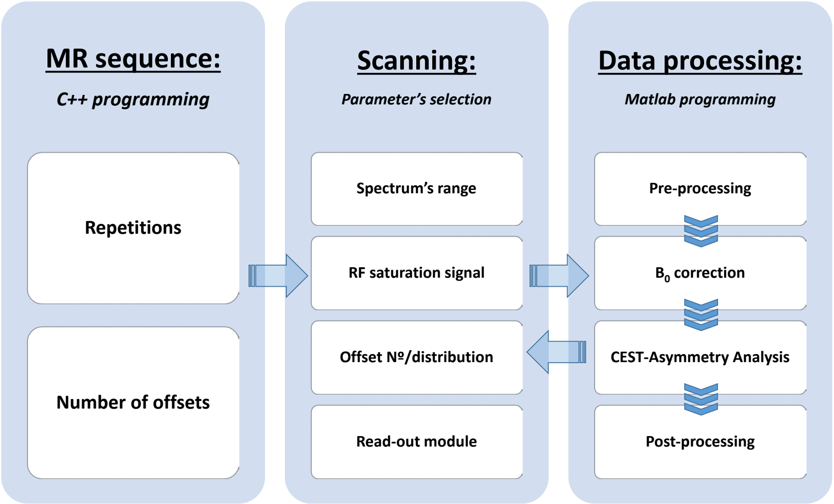

Fig. 4-1: Tasks organization for the Dynamic CEST imaging study

Those tasks implicated in each part of the following process description will be highlighted for quickly visualization of the reader.

4.1. Dynamic study

The principle muscles involved in this plantar flexion exercise are the ones located in the posterior side of the leg. They are the soleus muscle, the medial gastrocnemius (MG) and lateral gastrocnemius (LG), depicted in Fig. 4-2.*a*. Cr level are expected to increase primarily in the soleus and gastrocnemius muscles during plantar flexion exercise.[8]

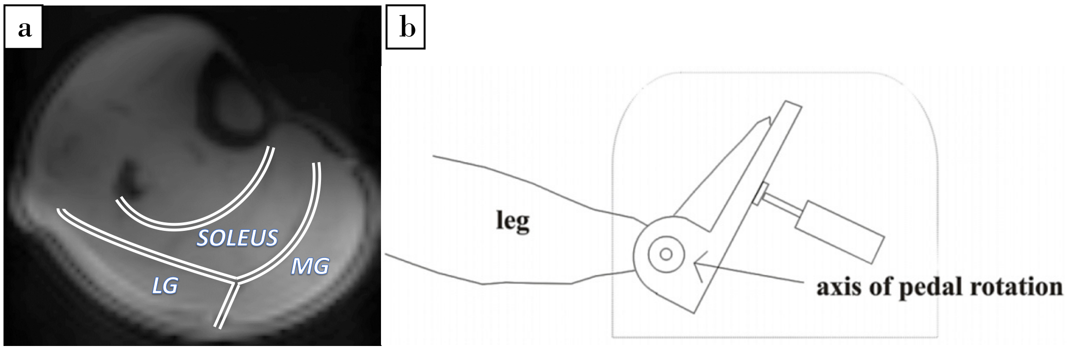

Fig. 4-2: a: Anatomical MR image of calf muscles manually segmented. Soleus, medial gastrocnemius [MG] and lateral gastrocnemius [LG]

b: Plantar flexion exercise: Position of the axis of pedal rotation in relation to the ankle.[23]

The dynamic CEST experiment in vivo was performed using a pneumatic ergometer as depicted in *Fig. 4-2.b*. It consisted of 2 min of rest, 6 min of plantar flexion exercise at a pedal pressure of 1.8 bars and 4 min of recovery (total of 60 repetitions). Free Cr mapping with 13 offsets, frequency shift of 1.8 ppm, spectral range of ±2.8 ppm and delta frequency of 1.2 ppm (integration range = 1.2-2.4 ppm). The matrix size was 64×64 and field of view (FOV) 140×140 mm.

Siemens has provided a special Work-in-Progress CEST MR Sequence for the MR Center, which means that this sequence is not yet a product and can be used for research only. This MR sequence has a graphical user interface, which allows the adjustment of all parameters, including those specific for the CEST contrast. In *Fig. 4-3* the parameters that are available for optimizing the CEST module are illustrated (those not used have been pixelated):

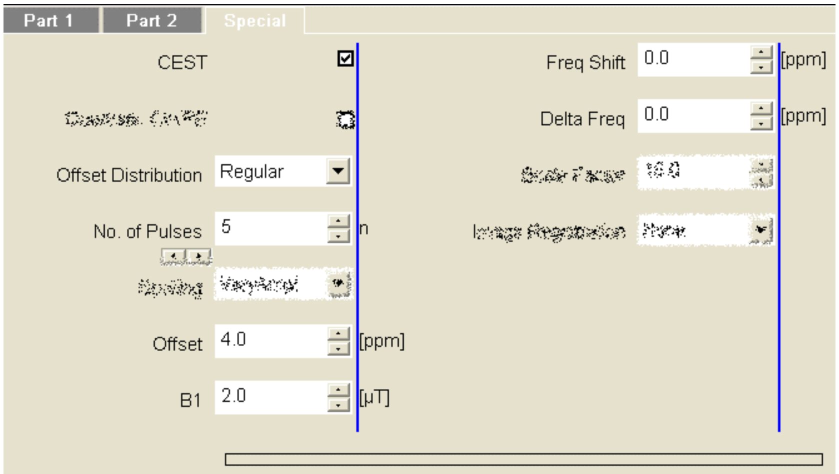

CEST ☑

Offset Distribution Regular

No. of Pulses 5 n

Offset 4.0 [ppm]

B1 2.0 [µT]

Freq Shift 0.0 [ppm]

Delta Freq 0.0 [ppm]

Fig. 4-3: Parameters available in the CEST module user interface

The parameters involved in the sequence optimization are:

- *CEST*: Flag activating the CEST-specific suppression pulses and triggering the image reconstruction according to CEST experiments.
- *Offset Distribution*: It defines the temporal pattern of frequencies (offsets) in which the different CEST saturation pulses are applied in the spectrum. The first measurement is acquired un-saturated (S_0), the rest are taken after saturation B_1^+ is applied:
    - *Regular*: Offsets are sampled with linear increments of pulse saturations from negative to positive frequencies in the frequency range specified by the variable "Offset"
    - *Alternating*: Offsets are sampled alternatively (negative/positive frequencies) starting from highest negative one (at -"Offset" ppm) till the last scan at 0 ppm
- *Saturation train of pulses (B_1^+) parameters: Collection of variables defining the saturation signal:*
    - *Nº of pulses:* Number of pulses applied during the CEST suppression module

  - *Pulse duration:* Length of each CEST suppression [ms]
  - *Interpulse delay:* Time between each CEST suppression pulse [ms]
- Offset: Positive limit of the spectrum. Range defined by ±*Offset*
- B1: Amplitude of each CEST suppression pulse [μT]
- Freq Shift: Resonance frequency of the target metabolite at which the saturation is applied (1.8 ppm for free Cr)
- Delta Freq: Frequency interval over which signal is integrated at symmetric sides of the Z-spectrum around the specified target resonance frequency "*Freq Shift*"

A graphical schematic of a Z-spectrum and how some of these parameters are defined for the CEST asymmetry analysis are illustrated in *Fig. 4-4*. The measured spectral points depicted as red circles in *Fig. 4-4*, at which the CEST saturation pulses are applied at different frequencies, are referred to as "offsets".

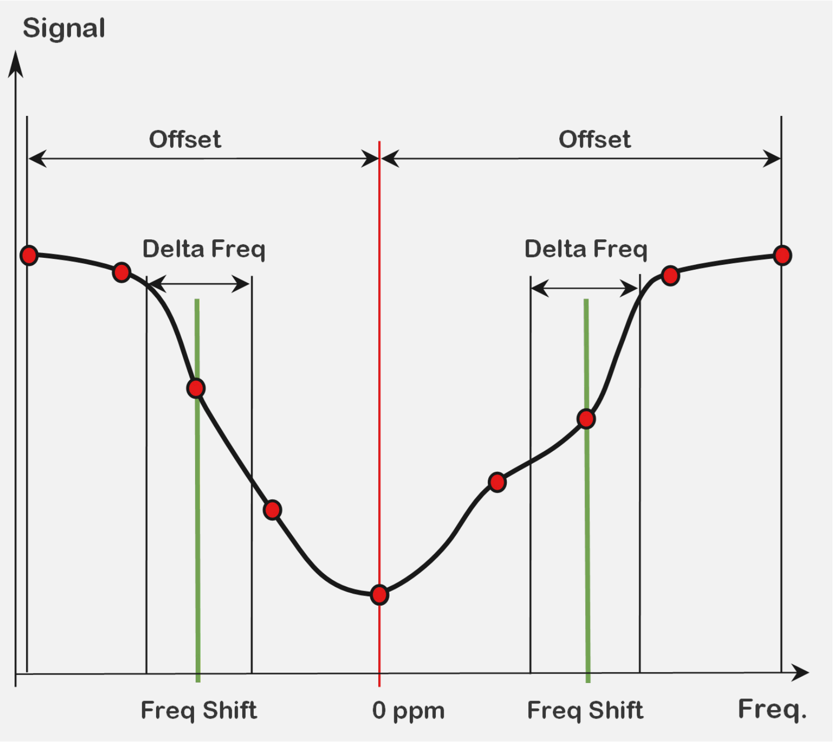

Fig. 4-4: Schematic of Z-spectrum and parameters used for CEST effect calculation

4.1.1. <u>MR sequence</u>

The tasks involved in this section are the ones highlighted in *Fig. 4-5*:

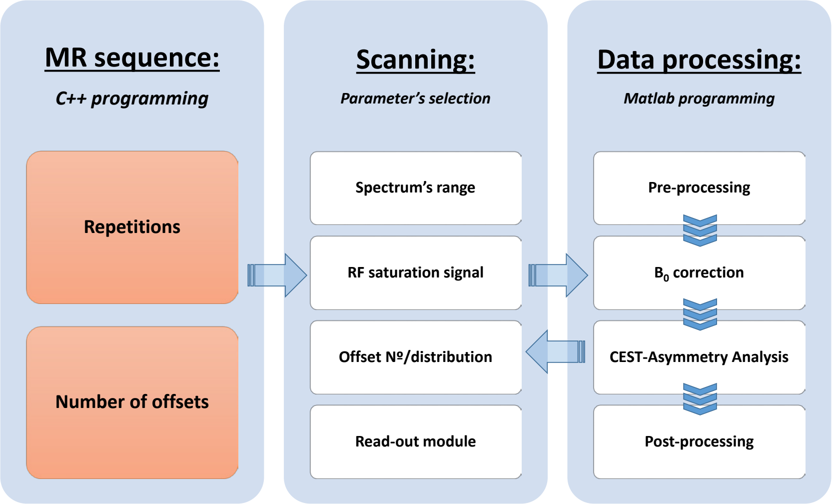

Fig. 4-5: Tasks involved which require MR sequence programming

Initially only one complete static CEST experiment including multiple "offsets" was implemented within the spectral range.

To be able to perform a dynamic study on muscle energetics a new parameter "Repetitions" had to be introduced in the graphical user interface, as shown in *Fig. 4-6*. Subsequent changes in the sequence programs were made so the static protocol was repeated automatically a number of times and the output images in DICOM format were stored properly.

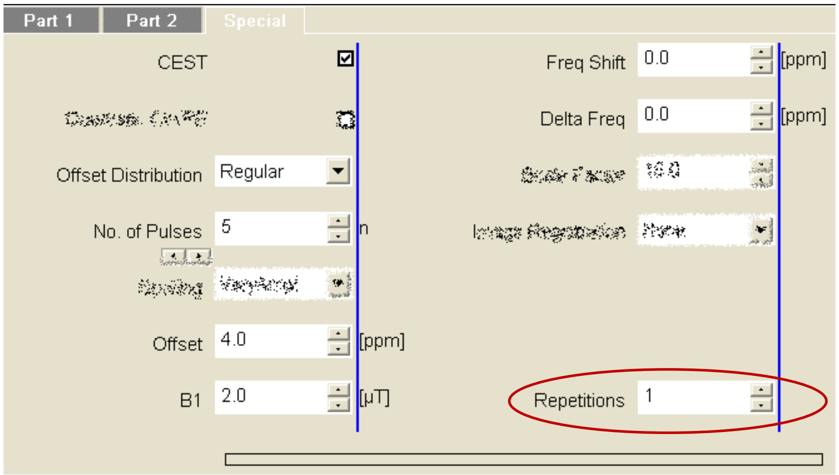

CEST ☑
Offset Distribution Regular
No. of Pulses 5 n
Offset 4.0 [ppm]
B1 2.0 [µT]
Freq Shift 0.0 [ppm]
Delta Freq 0.0 [ppm]
Repetitions 1

Fig. 4-6: Parameters available in the CEST module user interface

There was also a limitation in the total number of measured points per sequence (now Repetitions × Nº offsets × Nº slices) which also needed to be overcome. Previously only 13 offsets + 1 non-saturated = 14 measurements were acquired per slice for GAG-CEST evaluation.

4.1.2. Processing Tool

The tasks involved in this section are the ones highlighted in *Fig. 4-7*:

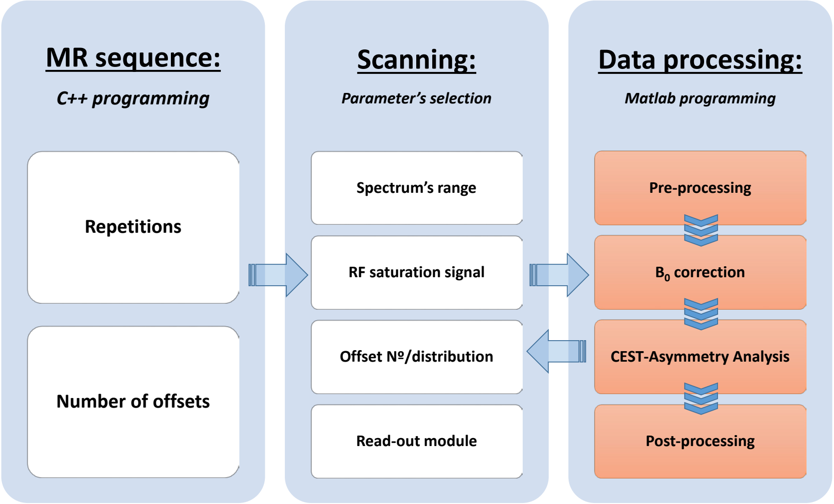

Fig. 4-7: Tasks involved which require Matlab programming for data processing

The raw data acquired after the scanner measurements consist on a number of DICOM images (one for each offset/measured point in the Z-spectrum). A diagram showing the stages during the data processing to finally achieve a CEST map is summarized in *Fig. 4-8*.

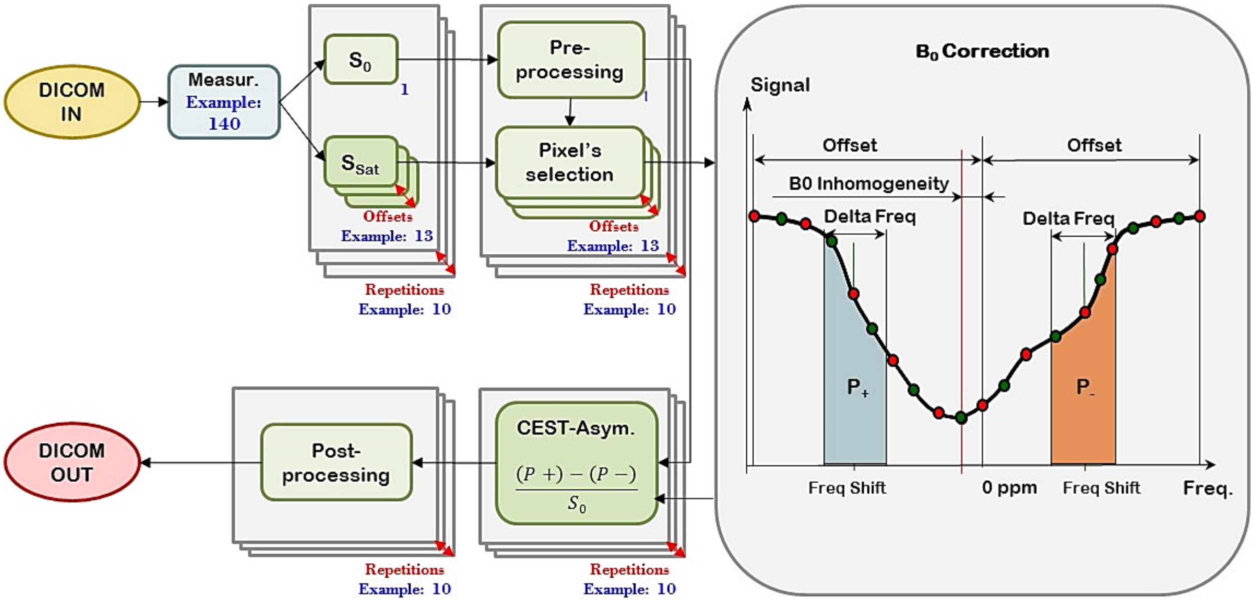

Fig. 4-8: Diagram of the stages followed for CEST map processing

The size of the variable stacks, multi-dimensional matrix depicted by green layers in *Fig. 4-8*, and the arithmetic of the technique had to be adapted in order to handle the new dimension "Repetitions" (grey layers). The details are covered in Section 4.2.

4.2. Cr-CEST mapping

Initially the Matlab tool provided was used as a black-box with a user interface panel to select the type of CEST map processing and the location of the raw DICOM files, see example in *Fig. 4-9*. During this thesis the interface panels, functions and data containers behind were analyzed and mapped to understand each step of the process. The Matlab functions, which correspond to the stages highlighted in *Fig. 4-7* and the example depicted in *Fig. 4-8*, are given as a simplified pseudocode.

To clearly distinguish between the start-up code and the new implementations, the applied changes are described between brackets and highlighted in green color.

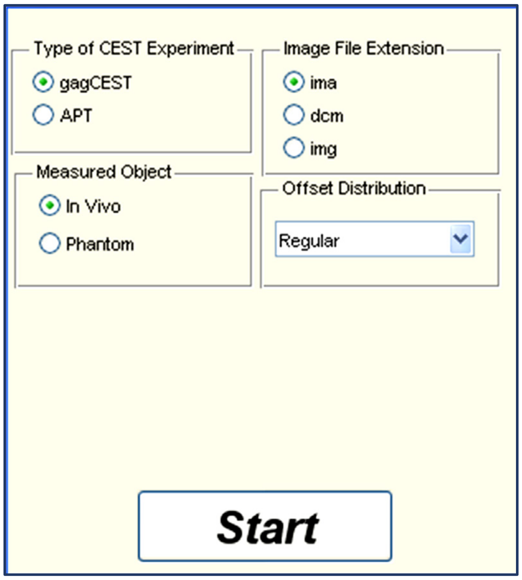
Type of CEST Experiment
● gagCEST
○ APT
Image File Extension
● ima
○ dcm
○ img
Measured Object
● In Vivo
○ Phantom
Offset Distribution
Regular

Fig. 4-9. Previous Matlab processing tool interface

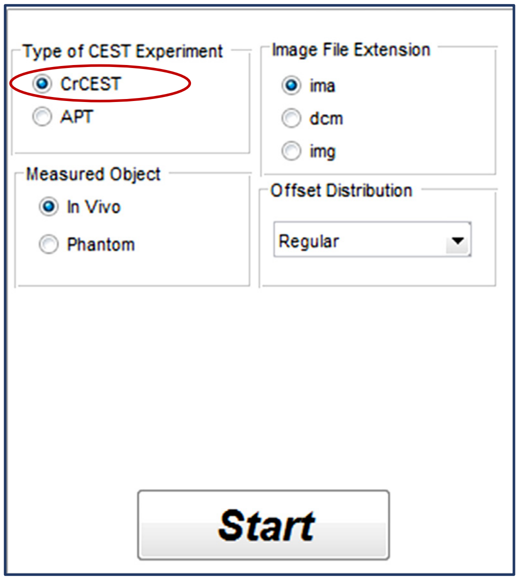
Type of CEST Experiment
● CrCEST
○ APT
Image File Extension
● ima
○ dcm
○ img
Measured Object
● In Vivo
○ Phantom
Offset Distribution
Regular

Fig. 4-10. Current Matlab processing tool interface

4.2.1. Processing Tool

The tasks involved in this section are the ones highlighted in Fig. 4-7, the function "Main" is the one calling the interface panel, showed in *Fig. 4-10*, and driving the outer layer of data processing shown in *Fig. 4-8*:

Pseudocode:

```
Function P1: Main

INPUT:  Type of CEST experiment, Type of File extension, Measured object,
        Offsets Distribution

OUTPUT: Intensity converted 2D CEST map in DICOM format

User selects Input parameters in the interface panel;
For all d DICOM image files do
    Load and filter DICOMS (d); [Read parameters values from DICOM metadata]
    Calculate Offsets frequencies array; [Increase array size for up-sampling
    points in $B_0$ correction]
    For each i slice do
        For each j [Dynamic repetition] do
```

```
                        Z-spectra calculation;
                        Spectra up-sampling; [Increase up-sampling points for curve
                        fitting]
                        Spectra curve interpolation/fitting;
                        Correct for B0 inhomogeneities; [Improved selection of water
                        saturation frequency]
                        Asymmetry analysis;
                        Post-processing; [Adding filter step, change contrast
                        formula]
                        / Export CEST mapping to DICOM format; [one for each j
                          Dynamic repetition]
            Endfor
        Endfor
Endfor
```

The function "Load and filter DICOMs" is in charge of creating the data stacks from the DICOMs, splitting between non-saturated/saturated measurements and make the first pre-processing of filtering and mask application to those voxels with low signal values.

Pseudocode:

```
Function P2: Load and filter DICOMs

INPUT:  Offsets Distribution

OUTPUT: N° of Slices, N° of Dynamic repetitions, N° of Offsets, Filtered non-
        saturated Stack ($S_0$),Filtered saturated Stack ($S_{sat}$), Max spectral frequency
        (Offset), Frequency Shift, Delta Frequency

User selects the directory where the dataset is stored;
User selects range of slices to be considered;
Count number of files → Total measurements
Check DICOM headers → Offsets, [N° of Offsets], [N° of Dynamic repetitions],
                      [Frequency Shift],[Delta Frequency]
For all d DICOM image files do
    Load DICOMS (d);
    For each i slice do
        Create stack corresponding to $S_0$;[Splitting also by Dynamic repetition(j)]
        If   Offsets Distribution=Regular then
             Create stack corresponding to $S_{sat}$ measured for linearly increasing
             frequencies;[Splitting also by Dynamic repetition(j)]
        Else  (Offsets Distribution=Alternating)then
             Create stack corresponding to $S_{sat}$ measured for alternating
             frequencies;[Splitting also by Dynamic repetition(j)]
        Endif
        For each j [Dynamic repetition]do
            Smooth filtering of $S_0$ Stack;
            Create mask with those voxels in $S_0$ which signal is lower than a
            certain threshold;
            Set to zero and label those voxels in $S_0$ and $S_{sat}$ stacks with low signal
            so they are not considered again for processing;
        Endfor
    Endfor
Endfor
```

The different arrays, which represent the *X* axis for the different spectra are calculated in the function "Offset array":

Pseudocode:

```
Function P3:  Offsets arrays
INPUT:  Max spectral frequency (Offset), Offsets Distribution
OUTPUT: Offsets frequencies array, Up-sampled offsets frequencies array, CEST_asym
        frequencies array

If   Offsets Distribution=Regular do
     Frequencies linearly distributed in range ±Offset → Offsets frequencies
     array;
     Up-sampled frequencies linearly distributed in range ±Offset → Up-sampled
     offsets array;[Increase array size for up-sampling points in B0 correction]
     Frequencies linearly distributed in range 0 to +Offset → Asym. analysis
     array;

Else (Offset Distribution=Alternating) then
     Frequencies alternatingly distributed in range ±Offset → Offsets frequencies
     array;
     Up-sampled frequencies alternatingly distributed in range ±Offset → Up-
     sampled offsets array;[Increase array size for up-sampling points in B0
     correction]
     Frequencies linearly distributed in range 0 to +Offset → Asym. analysis
     array;
Endif
```

In the "Z-spectra and B0 correction" function the spectra are interpolated to a higher number of points and corrected for B0 inhomogeneities. B0 field homogeneity is especially important for CEST experiments performed in high and ultra-high fields (like the ones performed in this work at 7T), and it causes a shift of the z-spectrum.[22] This can be seen in the spectrum curve depicted in the B0 correction stage of *Fig. 4-8*.

Pseudocode:

```
Function P4:  Z-spectra and B0 correction
INPUT:  Measured object, Offsets frequencies array, Up-sampled offsets
        frequencies array, Filtered non-saturated Stack (S0), Filtered saturated
        Stack (Ssat)
OUTPUT: Corrected saturated Stack (Ssat), Stack storing water resonance frequency
        per voxel/repetition/slice

Z-spectra calculation Ssat/S0;
For each voxel x do
    If   Measured object=Phantom do
         linear curve interpolation from "Offsets" to "Up-sampled offsets"
         array;[Increase up-sampling points]
    Else (Measured object=In vivo) then
         Smooth spline interpolation from "Offsets" to "Up-sampled offsets"
         array;[Increase up-sampling points]
    Endif
    Find water resonance frequency in the "Up-sampled offsets" fitted
    curve;[Improved selection of water saturation frequency]
    Circular shift to curve so that the water resonance frequency is at 0 ppm;
    Interpolation back to previous resolution and assort;
Endfor
```

The function "Asymmetry analysis" is the one performing the integration for those offsets within the frequency range defined by "Freq delta" around "Freq Shift" for each Dynamic repetition:

Pseudocode:

```
Function P5:  Asymmetry analysis
INPUT:  Type of CEST experiment, Filtered non-saturated Stack ($S_0$), Corrected
        saturated Stack ($S_{sat}$),Frequency Shift, Delta Frequency
OUTPUT: CEST contrast map, Integration range

Asymmetry curve calculation($(S^+_{sat}-S^-_{sat})/S_0$);
If Type of CEST experiment=CrCEST do
    Find Integration limits of range Delta Frequency around Frequency Shift;
Else (Type of CEST experiment=APT) then
    Find Integration limits of range for Amide Proton Transfer;
Endif
Asymmetry analysis integration $(P^+_{sat}-P^-_{sat})/S_0$ → CEST contrast image;
```

Finally, just before the CEST images are exported in DICOM format, when headers are also filled, a final post-process is necessary to achieve the proper contrast within the required limits.

Pseudocode:

```
Function P6:  Post-processing
INPUT:  Type of CEST experiment, Stack with CEST difference for $CEST_{asym}$
OUTPUT: Post-processed CEST contrast map

[2D smoothing filtering of the stack with CEST difference for $CEST_{asym}$];
If Type of CEST experiment=CrCEST do
    Image scaling;[change contrast formula]
    Delimit voxel values against outsiders;
Else (Type of CEST experiment=APT) then
    Post-process for Amide Proton Transfer;
Endif
```

4.2.2. Analytical Tool

The output that the Matlab tool provided were just a CEST map, hence to be able to investigate the z-spectra in more detail, complementary Matlab functions were developed.

In order to visualize, if there was a real CEST effect in a certain area of the image, it was necessary to select a region of interest (ROI) and plot its spectrum (average and standard deviation). To have an idea of how good the B_0 shimming was performed (process prior to the scan measurement to homogenize B_0 within the sample volume), the width of the water resonance frequency peak need to be calculated.

Finally, to verify the efficiency of the saturation pulses, the ratio between the water signal at its minimum with respect to its baseline was calculated as a percentage.

In summary, the new application corresponding to "***Function A1***", allow for one repetition:

- ✓ The selection of ROI by the user.
- ✓ Show the spectrum with the average and the standard deviation of the selected ROI
- ✓ Calculate the line width of the water resonance
- ✓ Calculate efficiency of the direct saturation (DS)

Function A1: **ROI spectrum, Shimming & Saturation efficiency**

```
INPUT: Max spectral frequency (Offset), Up-sampling rate

OUTPUT: Spectrum plots, $H_2O$ resonance frequency, line width, Saturation efficiency
        [%]

User selects the folder of CEST dataset;
Count the number of DICOM files;
Calculation of Offsets frequencies array;
Load, normalization and plotting of the last saturated measurement;
User selects a big area of interest within the object;
Intensity adjustment according to user's selection histogram (just for
visualization);
User selects the ROI to calculate Average and Std. deviation across the spectrum;
Drawing a red mask with the borders of the ROI selected;
For each ROI do
     For all offsets within the spectrum (d=2-end) do
         Calculation of 2D-mean and 2D-standard deviation;
     End for
     Spline curve interpolation from "Offsets" to "Up-sampled offsets" array;
     Find water resonance frequency in the "Up-sampled offsets" fitted curve;
     Calculation of water resonance line width "$\Delta v_{1/2}$" and saturation efficiency;
Endfor
Plot full spectrum, and a zoom-in area with the water resonance peak;
Print results: water resonance frequency, line width, Saturation efficiency [%];
```

As it was mentioned in Section 0, Siemens has its own software for CEST mapping reconstruction (ICE), but it does not allow reconstruction of repeated measurements for dynamic studies. To compare the Matlab processing tool and Siemens ICE, "*Function A2*" was implemented. It was used to adjust the filtering values in the post-processing stage, see Fig. 4-8.

This code was also adapted to allow comparison of CEST effect prior vs. after exercise in a dynamic study.

Function A2: **ICE VS Matlab CEST mapping**

```
INPUT: Siemens ICE mapping DICOM, Matlab processing tool DICOM

OUTPUT: 2D contrast plots, 2D comparison plots

User selects the folder of ICE mapped DICOM;
Load of DICOM;
2D image plotting;
User selects the folder of Matlab mapped DICOM;
Load of DICOM;
2D filtering of Matlab CEST image if necessary;
Plots of 2D CEST contrast images (ICE & Matlab);
Calculation of difference and ratio as a percentage;
Plots of CEST contrast differences and ratios [%];
```

For biological tissue it may not be clear, if creatine is sufficiently concentrated. Thus, a voxel scanning through the image is preferable, however ROI selection is the best option for delimited homogeneous samples within a phantom. "***Function A3***" was developed to allow voxel/ROI data selection and include an exporting feature to store the results to Excel. The last data treatment, such as data representation and statistical analysis shown in Section 5.3, is performed using Microsoft Excel 2013.

```
Function A3:  Voxel/ROI spectrum, Asymmetry analysis & Excel exporting

INPUT:   Corrected saturated Stack ($S_{sat}$), Stack with CEST difference for $CEST_{asym}$,
         Max spectral frequency (Offset), Offsets frequencies array, $CEST_{asym}$
         frequencies array, Integration range

OUTPUT:  Spectrum plots, Asymmetry curve plots, Spectrum table, Asymmetry table

User selects the dynamic repetition, ROI/voxel processing, N° of desired ROI's,
Fixed ROI's or selected by user, Plotting=true/false;
If data processing=voxel_based do
    Select distance between voxels to consider;
    Horizontal scanning, row by row;
    If Plotting=true AND voxels in $S_{sat}$ stack overcome a certain threshold do
       Plot voxel full spectrum with integration areas;
       Plot voxel asymmetry curve calculation($(S^{+}_{sat}-S^{-}_{sat})/S_0$) with integration area;
       Show MR image and alternatively a mask with the previous scanned voxels
       (yellow) and current one (red);
    End if
Else (data processing = ROI_based) then
    Select number of ROI's to consider;
    For each ROI do
        If ROI= selected by the user do
           User selects the ROI;
           If Plotting=true do
              Plot averaged ROI spectrum with integration areas;
              Plot averaged ROI asymmetry curve calculation($(S^{+}_{sat}-S^{-}_{sat})/S_0$) with
              integration area;
              Show MR image with ROI selected in red color;
           End if
        Else(ROI= fixed areas)then
           Fixed areas within each sample;
           If Plotting=true do
              Plot averaged ROI spectrum with integration areas;
              Plot averaged ROI asymmetry curve calculation($(S^{+}_{sat}-S^{-}_{sat})/S_0$) with
              integration area;
              Show MR image with ROI selected in red color;
           End if
        / Export tables with averages samples/ROI's spectra and asymmetry curves
        into Excel;
        End if
    End for
Endif
```

4.3. Phantom experiments

The objective of the present thesis was to optimize an MR sequence and thereby maximize the contrast of Cr-CEST maps. There are several factors, which influence the CEST effect:[4, 22]

- Magnetic static field "B_0"
- Field homogeneity
- Metabolite concentration with chemical exchange
- Exchange rate "k_{sw}"

- Temperature
- pH
- T_1 relaxation of water protons
- RF saturation pulses “B_1^+”

Some of these factors can be considered to remain constant during the acquisition time, like B_0, temperature and T_1. Field inhomogeneity is corrected in Function P4: “Z-spectra and B_0 correction” described in Section 4.2.1.

The exchange rate “k_{sw}” is affected by the temperature, pH and molecular environment. Silvio Aime et al. found a linear relationship between an amide protons(-NH) complex in the pH range between 5.5 and 8.1.[24] Phillip Zhe Sun et al. also found an approximated linear pH CEST dependence for Cr amine protons ($-NH_2$) with a slope of 2% per pH unit at 3T and 8% per pH unit for 9.4T.[25]

The relation between creatine concentration [Cr] and CEST effect was linear for the experiments performed by Mohammad Haris et al. to study Creatine Kinase enzyme. The rest of the metabolites present in the reaction had no considerable CEST effect contribution due to their much slower exchange rate.[7]

RF saturation parameters, specially pulse length and amplitude also play an important role to control CEST contrast, spillover effect, width of CEST peaks and saturation efficiency.[7]

The phantom experiments are hence designed to study:

- ✓ The CK metabolites contribution to CEST effect
- ✓ The pH contribution to CEST effect

The MR sequence is a variant of a rapid imaging gradient echo technique, known as FLASH (Fast Low Angle Shot Imaging) developed by Haase et al. in 1986 [26], which involves short echo times (TE), short repetition times (TR) and spoiled Gaussian saturation pulses.

Two different readout modules (placed just after the CEST saturation pulses) with different segmentations of k-space trajectories are also compared (see the experiments design depicted in *Fig. 4-12* and *Fig. 4-13*). It will be shown in Section 5.3 how the reduction of the readout period by trajectory’s segmentation may affect the Z-spectra and the Asymmetry analysis results. For more detailed reading about k-space please refer to Section 2.3.5.

The tasks involved in this section are the ones highlighted in *Fig. 4-11:*

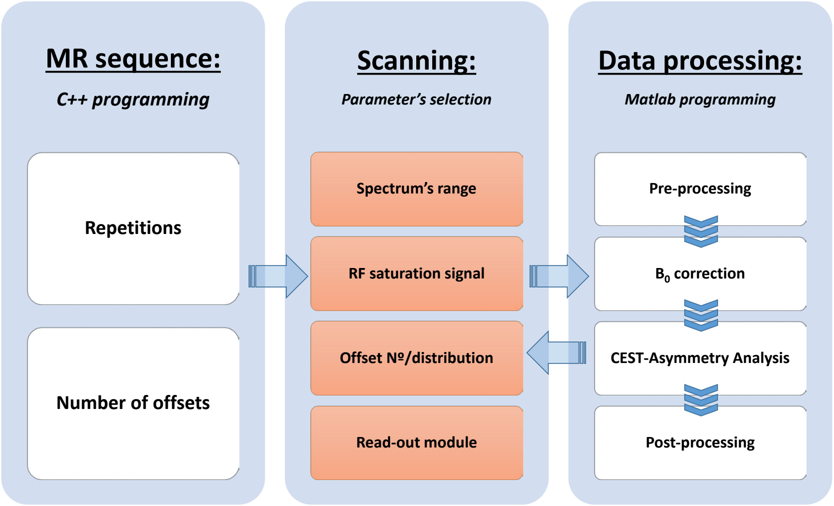

Fig. 4-11: Tasks involved which require parameter's selection for sequence optimization

4.3.1. CK metabolite contributions to CEST effect

In order to mimic the CK metabolites evolution in muscle during mild exercise, the 6 samples defined in *Table 4-1* have been prepared with a total agent's concentration of 50 mMol/l:

Tube	Content	
1	100%	Cr
2	25% 75%	PCr Cr
3	50% 50%	PCr Cr
4	75% 25%	PCr Cr
5	100%	PCr
6	100%	Pi

Table 4-1: Metabolites concentration of the samples used to analyze their CEST contribution

where *Pi* is the inorganic phosphate coming from the phosphate salts used to prepare the PBS solution described in the materials Section 3.2. The purpose to include this solution is to prove that the buffer solution does not influence the CEST measurement due to its symmetric Z-spectra.

The diagram depicted in *Fig. 4-12* show the design of the experiments to study how the saturation pulse parameters (Length and FA) and k-space readout module affect the CEST contrast for different CK metabolite concentration.

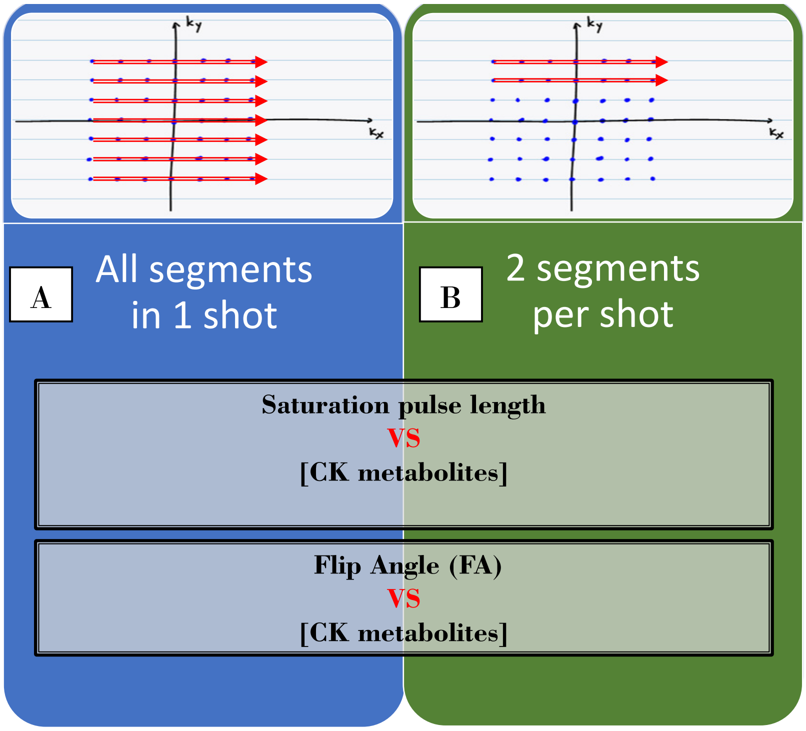

Fig. 4-12: Experiments design regarding CK metabolites CEST contribution

The default parameters are defined as follows:

- Spectrum range = ± 3.5 ppm
- Saturation pulses number and length = 5 pulses, 100 ms each
- FA[1]= 8°
- B_1^+ Amplitude = max to fulfill SAR[2] limits.- Range = $[3.0\text{-}3.8\ \mu T]$
- N° of offsets = 127 for readout module A
- N° of offsets = 63 for readout module B
- Resolution = 128×128 for readout module A
- Resolution = 64×64 for readout module B
- Offsets distribution = Regular
- Phase encoding reordering = Central
- Temperature = 25 °C
- pH = 7
- Frequency shift = 1.8 ppm

Phase encoding reordering define the order in which segments are measured in the k-space. Central means that the first ones are close to the K_x axis, hence starting to acquire central k-space lines immediately after the CEST saturation module was applied and outer k-space lines later.

---

[1] This flip angle refers to the pulses used for the readout module, not to the pulses used during saturation period

[2] SAR stands for Specific Absorption Rate which is defined as the power absorbed by the human body when is exposed to a RF electromagnetic field

Finally a MRS analysis was performed to the same samples containing Cr and PCr as the classical technique to study muscle energetics in vivo.

4.3.2. pH contribution to CEST effect

In order to understand the effect of pH in the physiological range for mild exercise the 6 samples defined in *Table 4-2* have been prepared with a fixed Cr concentration of 50 mMol/l and a linearly increasing pH distribution:

Tube	**1**	**2**	**3**	**4**	**5**	**6**
pH	**7,2**	**7**	**6,8**	**6,6**	**6,4**	**6,2**

Table 4-2: pH of the samples used to analyze their CEST contribution

The diagram depicted in *Fig. 4-13* shows the design of the experiments to study how the CEST saturation pulse parameters (Amplitude and FA), Offsets distribution, Phase encoding reordering and k-space readout module affect the CEST contrast for different pH.

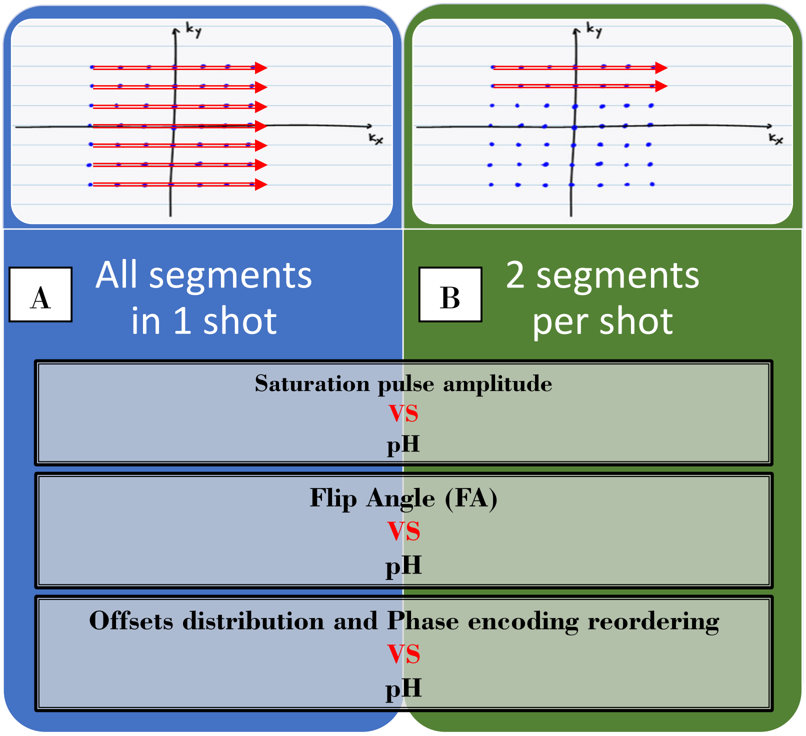

Fig. 4-13: Experiments design regarding pH CEST contribution

The rest of the parameters are the same as in 4.3.1.

5. RESULTS

This chapter summarizes the results obtained with the methods described in the previous chapter. The first part shows a simulation of the RF pulses and gradient timings employed as well as the reconstructed CEST maps of the dynamic exam. Secondly the results at intermediate steps during the data processing are presented. Finally a set of comparisons is shown to analyze Cr-CEST contrast evolution with (i) environmental factors and (ii) several MR sequence parameters.

5.1. Dynamic study

5.1.1. MR sequence

After the changes described in Section 4.1.1, the same sequence could be run for a number of repetitions for a dynamic study. *Fig. 5-1* shows an example of one repetition of the sequence used. S_0 corresponds to the acquisition with no saturation and S_x to the 5 acquisitions after saturation pulses are applied:

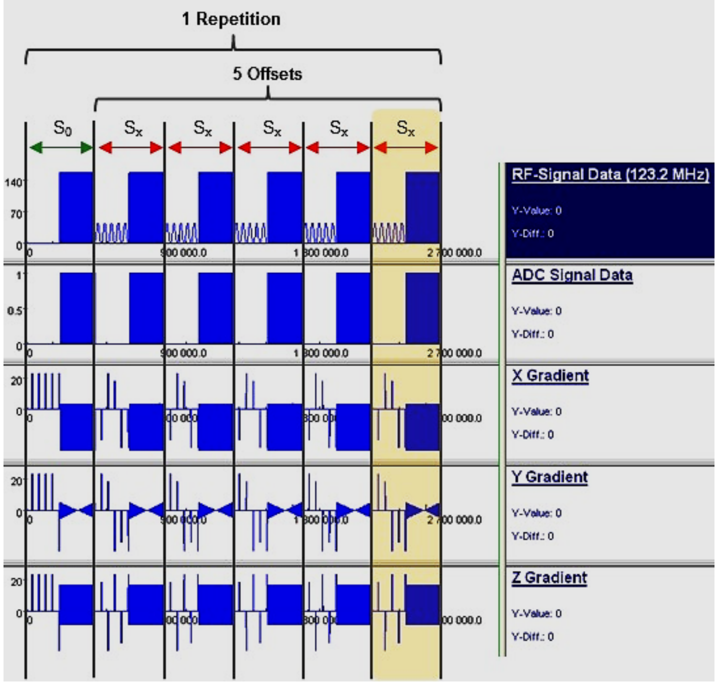

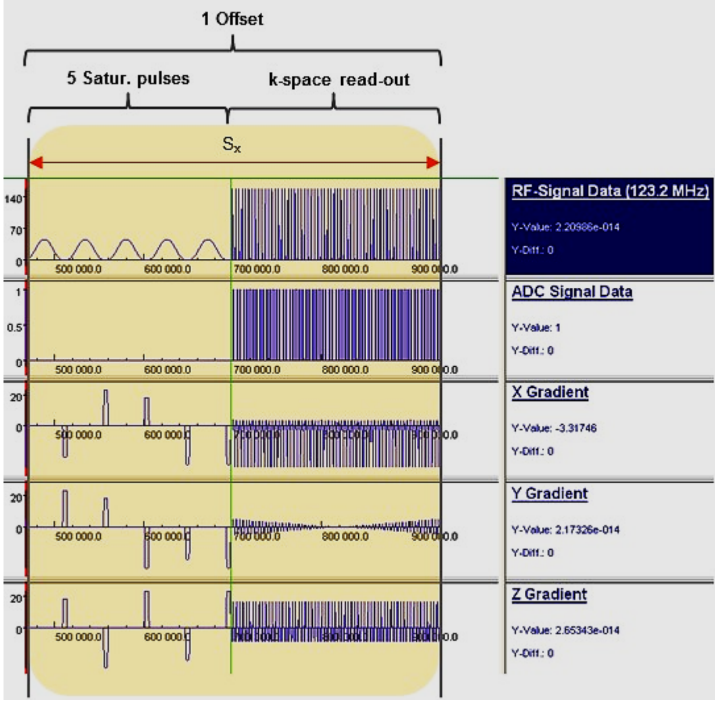

Fig. 5-1. Sequence simulation for 1 repetition with 5 offsets and 5 saturation pulses

5.1.2. Processing Tool

After the Matlab Processing Tool was modified, as described in Section 4.1.2, it was possible to perform a dynamic experiment and prove that it was achievable with the hardware and software available.

A total of 840 measurements were acquired for 1 slice of the calf muscles (1 non-saturated, 13 saturated at different offsets [between ±2.8 ppm] for 60 repetitions).

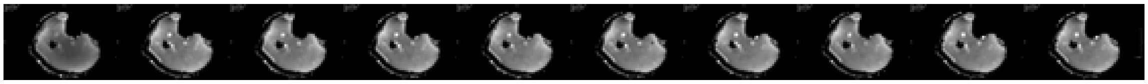

Rest period (2 min)

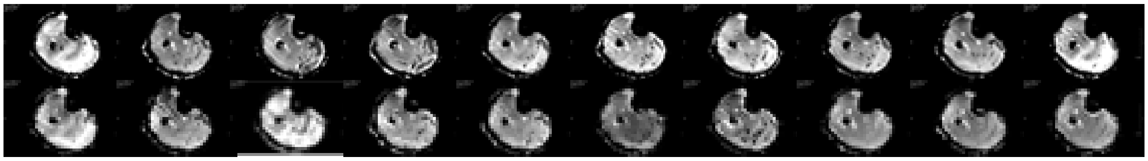

Plantar flexion exercise period (4 min)

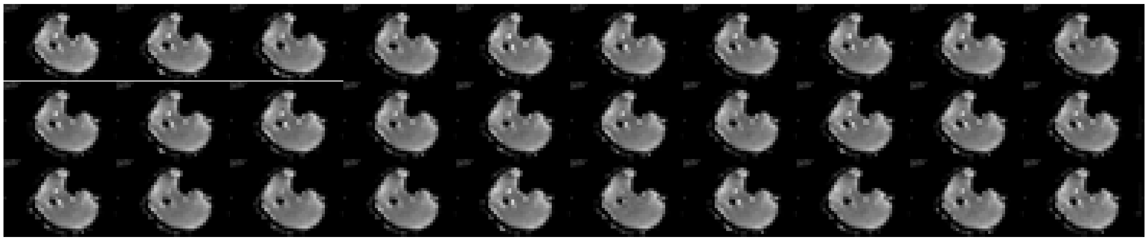

Recovery period (6 min)

Fig. 5-2: Cr-CEST maps for a dynamic exam (60 repetitions)

It is visible in *Fig. 5-2* that during exercise there are motion artifacts, but also bright areas with apparently high CEST effect. Unfortunately just after exercise there was no perceptible Cr decay expected. The physiological recovery after mild plantar flexion exercise (described by the CK kinetics) is in the range of seconds or few minutes [0 - 6 min].[8]

It was clear then that further analysis of the data processing and acquisition was needed.

5.2. Cr-CEST mapping

To evaluate how the modified Matlab functions assigned were performing through the processing stages described in *Fig. 4-8*, the three new functions described in Section 4.2.2 were implemented. The present section presents the results achieved by each of them on phantoms with the 6 samples as described in Section 4.3.

5.2.1. *<u>Function A1</u>: ROI spectrum, Shimming & Saturation efficiency*

This new application allowed the following features:

- ✓ The selection of regions of interest (ROI) by the user.
- ✓ Show the spectrum with the average and the standard deviation of the ROI's selected
- ✓ Calculate the line width of the water resonance peak

Fig. 5-3 shows the output figures corresponding to the Matlab Function A1.

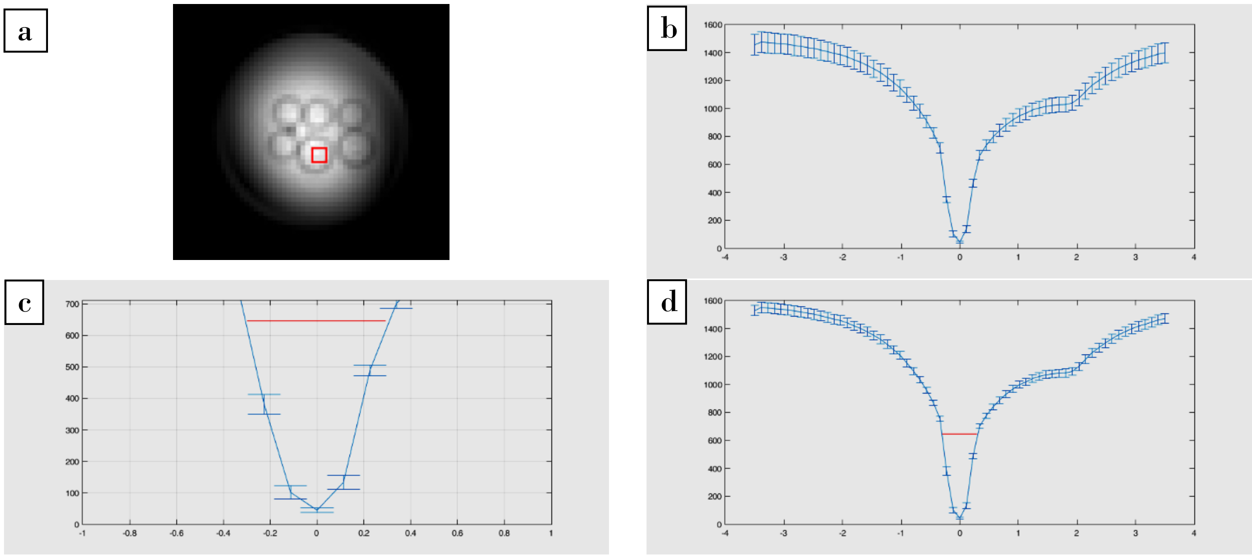

Fig. 5-3: Spectra, DS line width and saturation efficiency for the ROI selected by the user (3×3 voxels)
Sample corresponding to a solution of 50mM/l of Cr in PBS
(a) ROI selected by the user (3×3 voxels)
(b) Averaged and std. deviation of Z-spectrum (9 voxels covered by the ROI) across 63 offsets
(c) Visualization of the line width (length and position at half height of the peak)
(d) Zoomed window for better perception of the saturation efficiency

The *X* axis represents the frequency in ppm and the *Y* axis represents the signal value in A.U. (arbitrary units); no normalization with respect S_0 is performed.

The following results are printed by the function into the command window:

```
Water Peak Width at half height is 0.59 ppm
Water Peak Min at 0.00 ppm is 43.00. 3.46% of baseline (1244.54)
```

5.2.2. __Function A2__: ICE VS Matlab CEST mapping

This function provides at first glance not only the CEST contrast achieved by the Siemens ICE and the Matlab Processing Tool applied to the same phantom showed in *Fig. 5-3*, but also the ratio between them.

The output figures corresponding to the Matlab *Function A2 outputs* look like the following:

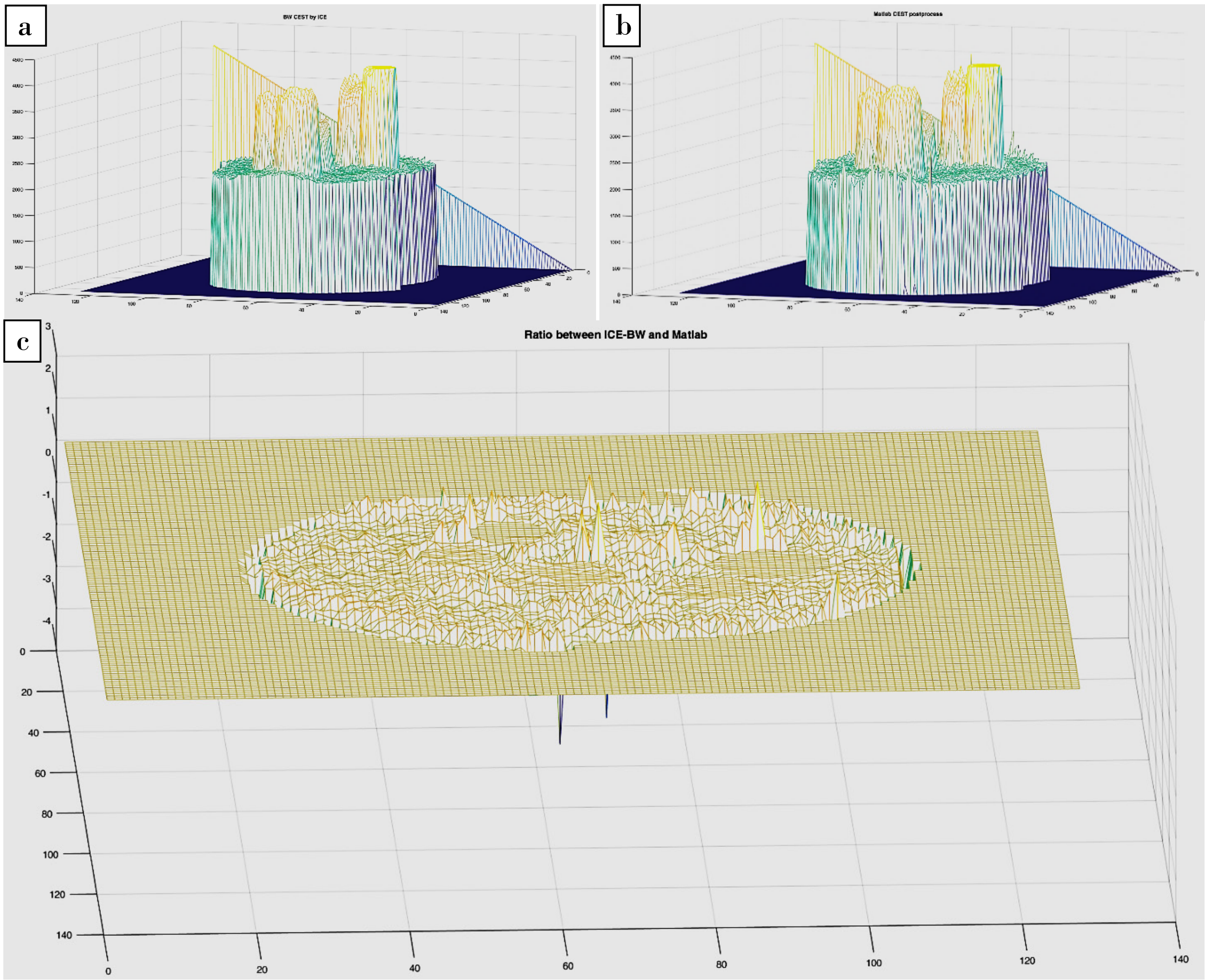

Fig. 5-4: Surface plots of the CEST maps reconstructed by Siemens ICE and the Matlab Processing Tool
(a) 2D surface plotting of the Black and White (BW) Cr-CEST map reconstructed map by ICE
(b) 2D surface plotting of the Cr-CEST reconstructed map by the Matlab Processing Tool
(c) 2D surface plotting of the ratio between both maps

The results are illustrated visually because the output values for Z-spectra, CEST asymmetry and finally image contrast will be arbitrary. Therefore it would not make much difference to calculate the exact difference for each of the sample contained in the phantom.

5.2.3. *Function A3*: *Voxel/ROI spectrum, Asymmetry analysis & Excel exporting*

As has been mentioned in Section 4.2.2, depending on the user's needs this function can run the data processing for single voxels or for certain areas. In case the voxel based processing is selected, a row by row scan is performed and the Z-spectra and asymmetry curves (i.e., subtraction of corresponding offsets on each side of the water resonance) are presented with the corresponding areas of integration for the subsequent contrast calculation.

The example presented in *Fig. 5-5* corresponds to the red voxel located approximately in the center of the phantom slice inside one of the syringes depicted in *Fig. 5-5.c*. The slice scanning has been parametrized to select one every 5 voxels.

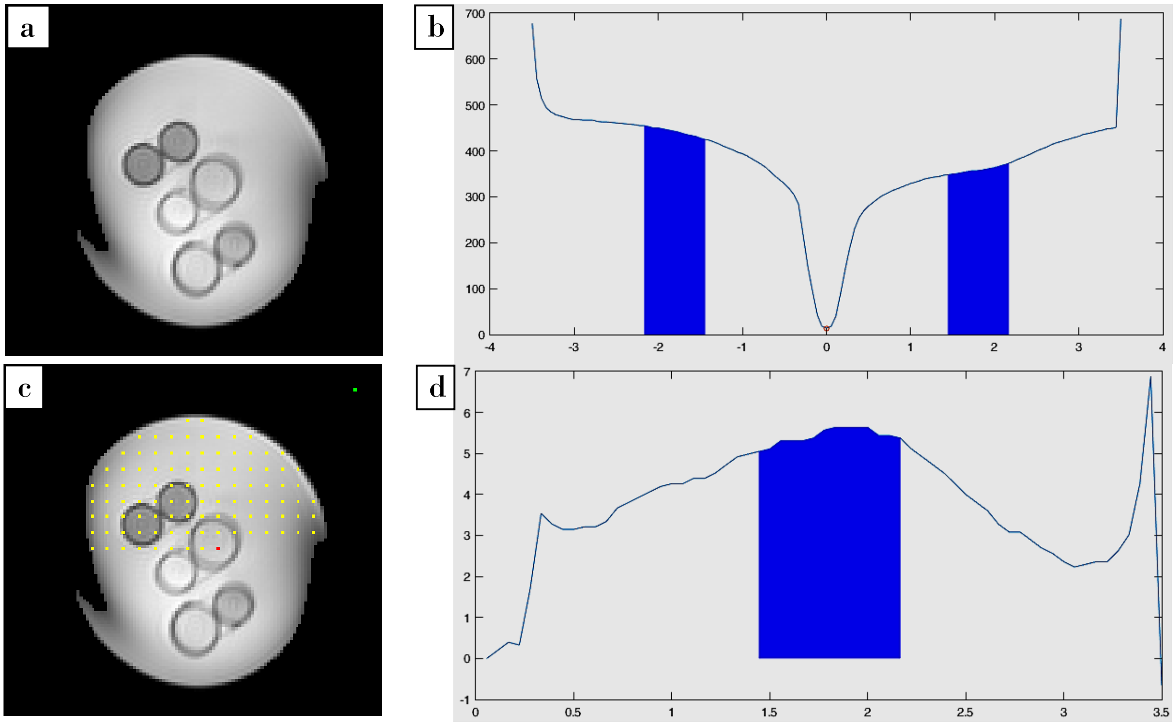

Fig. 5-5: Example of voxel based scan across a slice. Z-spectrum and Asymmetry curves with integration areas corresponding to the current voxel being analyzed, depicted in red color, are shown.
(a) MR image of the slice selected across a phantom with 6 samples/syringes
(b) Z-spectra with highlighted water resonance at 0ppm and integration areas after B_0 correction
(c) Superposition of the slice image and the previous and current voxels being analyzed
(d) Asymmetry curve and integral range for future contrast calculation after B_0 correction

To detect more easily if the B_0 correction was done properly, the value at 0 ppm is highlighted to check if it really corresponds to the center of the water resonance peak.

For the phantom tests shown in Section 5.3, ROI selection was preferred due to theoretical homogeneity of the solutions within each sample. The example presented in *Fig. 5-6* corresponds to the ROI selected by the user depicted in red color.

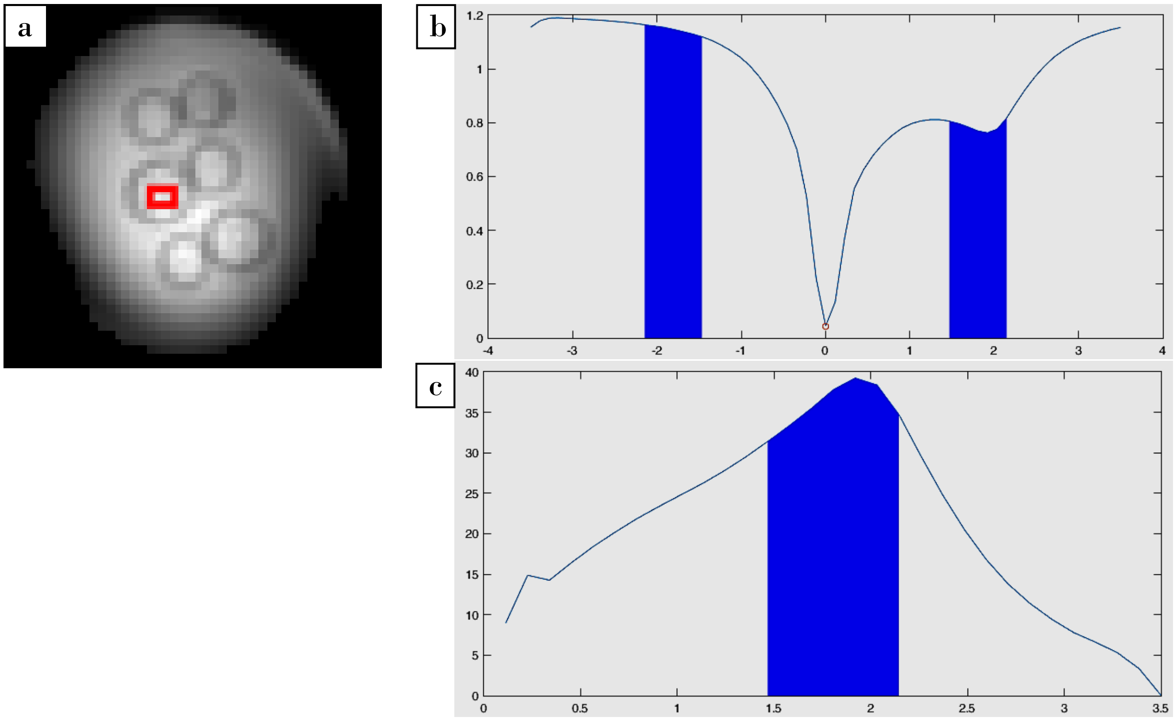

Fig. 5-6: Example of a user selected ROI evaluation within the slice. Z-spectrum and Asymmetry curves with integration areas.
(a) MR image of the slice and the ROI selected by the user depicted in red color
(b) Z-spectra with highlighted water resonance at 0ppm and integration areas after B_0 correction
(c) Asymmetry curve and integral range for future contrast calculation after B_0 correction

The last feature included in "***Function A3***" was the export of tables into an Excel file with the data corresponding to the Z-spectra and Asymmetry evaluation. This feature was triggered when the ROI's were defined previously as voxel coordinates of opposite rectangle/square corners for each sample.

After exporting the tables, the last data processing steps, such as contrast calculation, data representation and statistical analysis were performed directly in Excel. The example presented in *Fig. 5-7* corresponds to fixed ROIs within the 6 samples and the tap water filling the phantom.

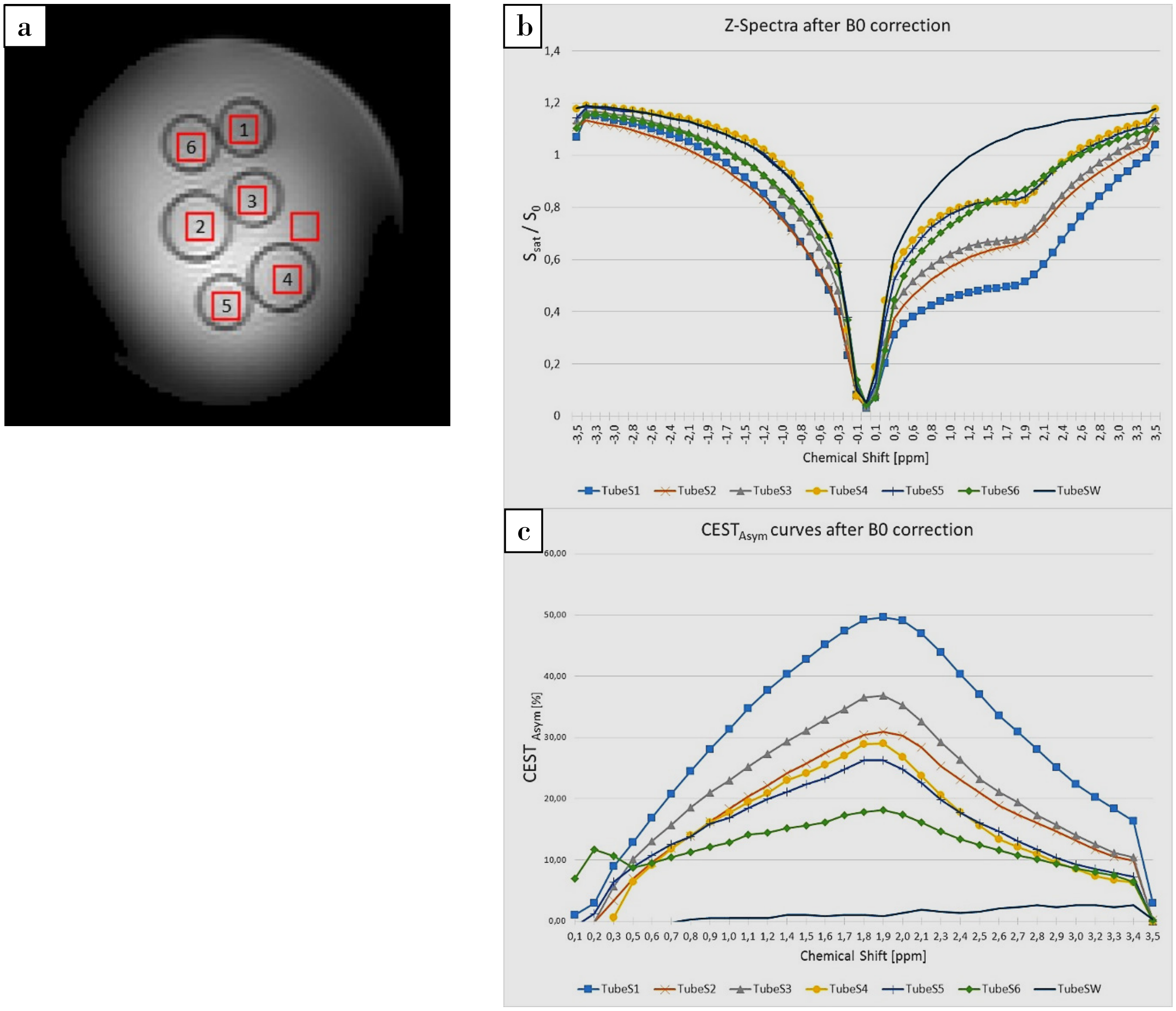

Fig. 5-7: Example of fixed selected ROIs evaluation within the slice. Z-spectrum and Asymmetry curves for each of the samples are presented.
(a) MR image of the slice and the fixed ROIs selected are depicted in red color
(b) Z-spectra after B_0 correction for each ROI
(c) Asymmetry curves after B_0 correction for each ROI

5.3. Phantom experiments

The purpose was now to test the sensitivity and specificity of CEST detection from free Cr by changing the Cr concentration and pH.

The following results compare the evolution of each of the samples defined in Section 4.3 with different sequence parameters. Each series corresponds to an ROI of 3×3 voxels placed inside the samples as depicted in *Fig. 5-7.a*.

5.3.1. CK metabolites contribution to CEST effect

To facilitate the comparison between samples and sequence parameters, the final results are presented as the final CEST maps contrast, expressed in A.U. However the Z-spectra and $CEST_{asym}$ curves provide more detailed information. *Fig. 5-8* shows the Z-spectra for the same samples, same conditions and almost the same sequence (except for the readout module). *Fig. 5-9* shows the same comparison, but for the CEST_{asym} curves.

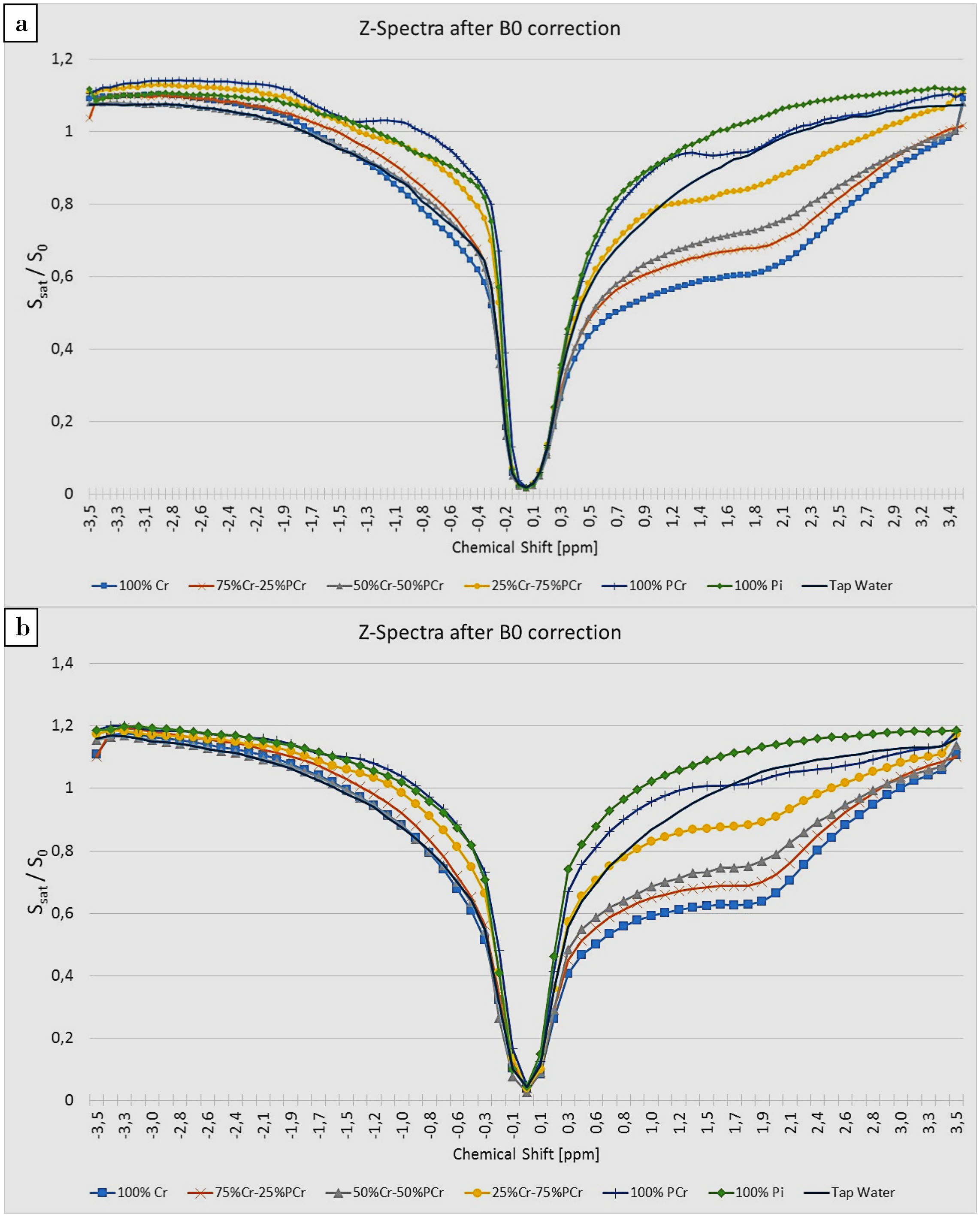

Fig. 5-8: Z-Spectra acquired with different readout modules. (FA=1°, 5 pulses of 100 ms)
(a) Readout module where all segments are read in 1 shot.- B_1^+ Amplitude = 3.5 µT
(b) Readout module where 2 segments are read per shot.- B_1^+ Amplitude = 3.0 µT

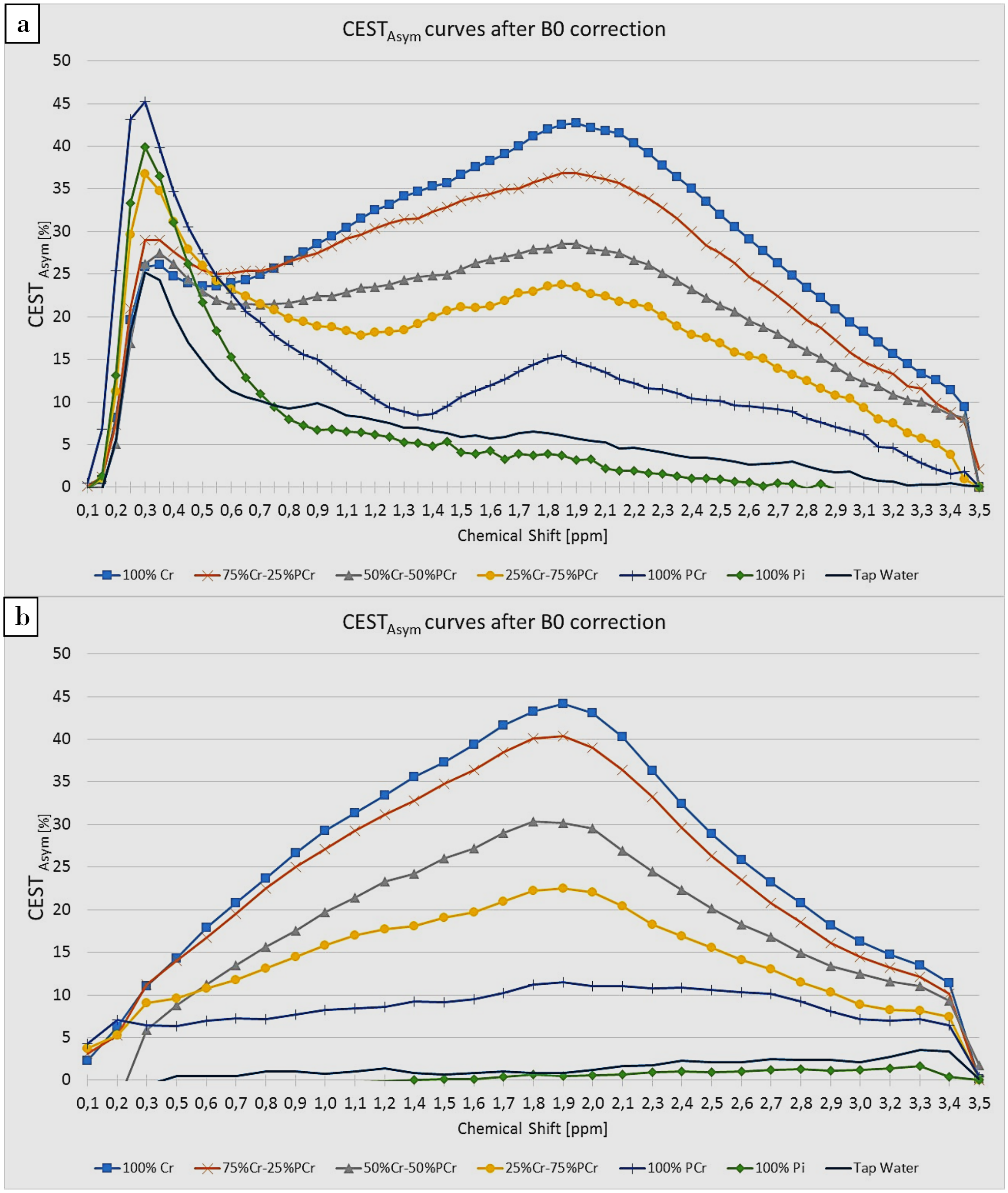

Fig. 5-9: CEST_{Asym} curves acquired with different readout modules. (FA=1º, 5 pulses of 100 ms)
(a) Readout module where all segments are read in 1 shot.- B_1^+ Amplitude = 3.5 µT
(b) Readout module where 2 segments are read per shot.- B_1^+ Amplitude = 3.0 µT

Fig. 5-10 presents as a summary, the contrast achieved by the solutions with different concentrations of CK metabolites and how they are affected by three different FA: 1º, 5º and 9º. Linear trend lines are calculated for those samples containing free Cr to find the relation between Cr concentration and contrast, their formulas are also provided.

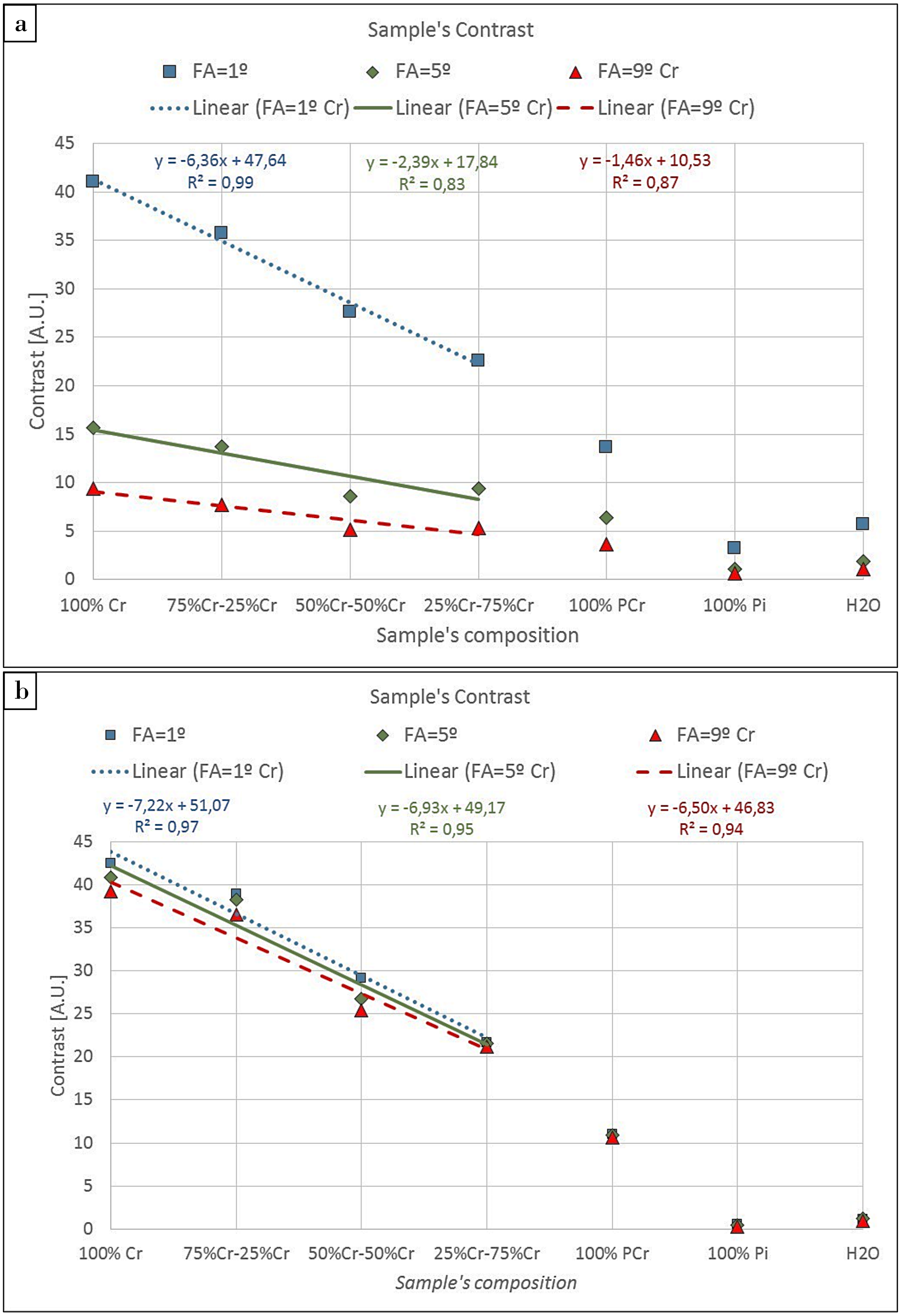

Fig. 5-10: Contrast achieved with different readout modules. (FA vs. [Cr])
(a) Readout module where all segments are read in 1 shot.- B_1^+ Amplitude = 3.5 μT
(b) Readout module where 2 segments are read per shot.- B_1^+ Amplitude = 3.0 μT

Fig. 5-11, on the other hand shows how the same samples are affected by three different B_1^+ pulse lengths, 100, 90 and 80 ms. Linear trend lines and their formulas are also calculated for those samples containing free Cr.

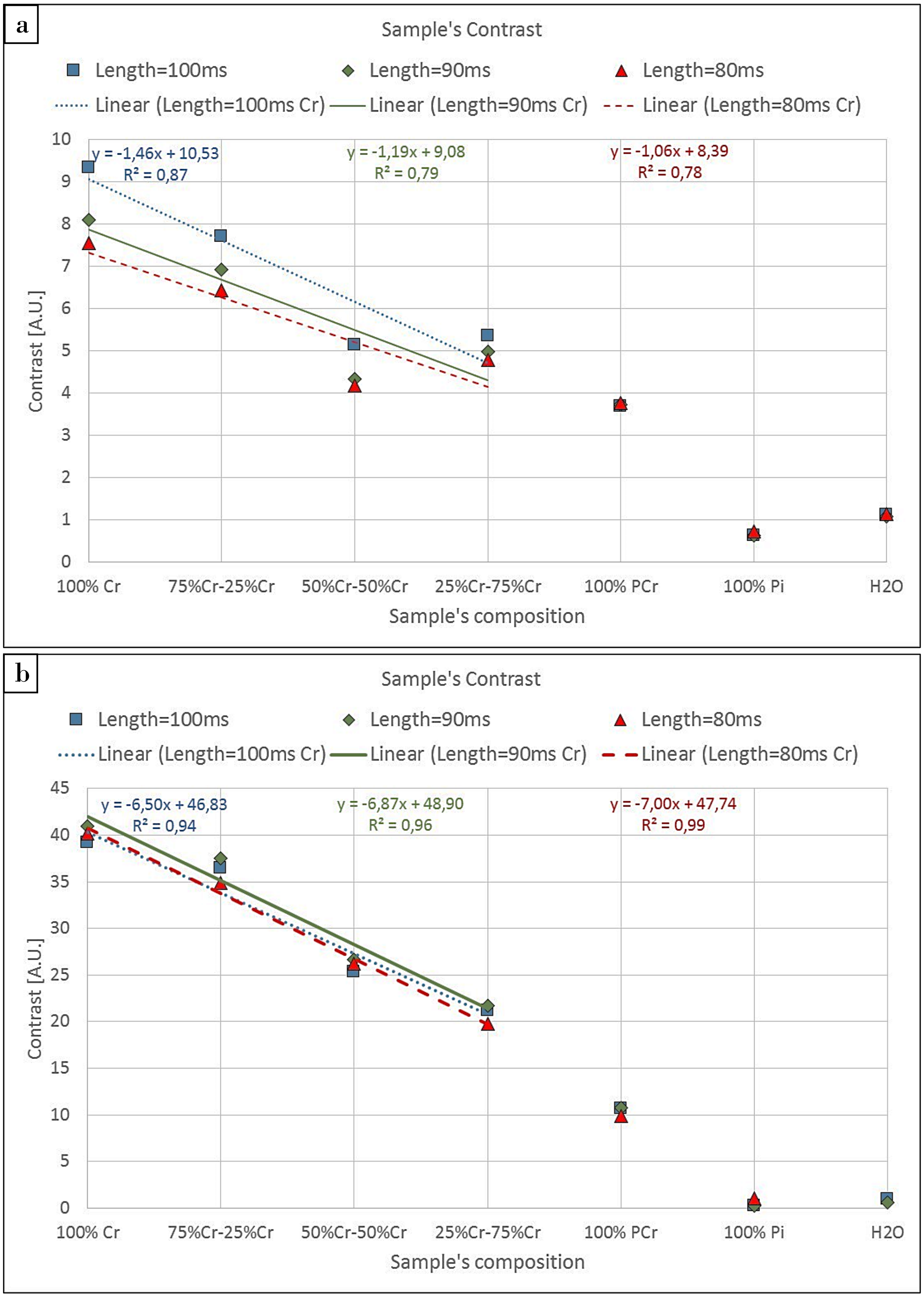

Fig. 5-11: Contrast achieved with different readout modules. (Pulse lengths vs. [Cr])
(a) Readout module where all segments are read in 1 shot.- B_1^+ Amplitude = 3.5 μT
(b) Readout module where 2 segments are read per shot.- B_1^+ Amplitude = 3.0 μT

^{31}P-MRS is currently the gold standard technique to determine the CK activity and a proven tool to study metabolic abnormalities such as skeletal muscle disease (muscular dystrophy).

The next results make use of MR Spectroscopy to show the evolution of PCr (measurable by both ^{31}P-MRS & ^{1}H-MRS) and free Cr (measurable only by ^{1}H-MRS). Remember that during exercise PCr was split into free Cr and ATP is produced due to the following reaction taking place in vivo:

$$ADP + PCr + H^{+} \overset{CK}{\leftrightarrow} Cr + ATP \tag{1.1}$$

Fig. 5-12 shows the evolution of samples with different concentrations between Cr and PCr. The values presented in *Fig. 5-12.a* represent the area under the peaks shown in *Fig. 5-12.b* and *Fig. 5-12.c* measured by ^{31}P-MRS and ^{1}H-MRS respectively.

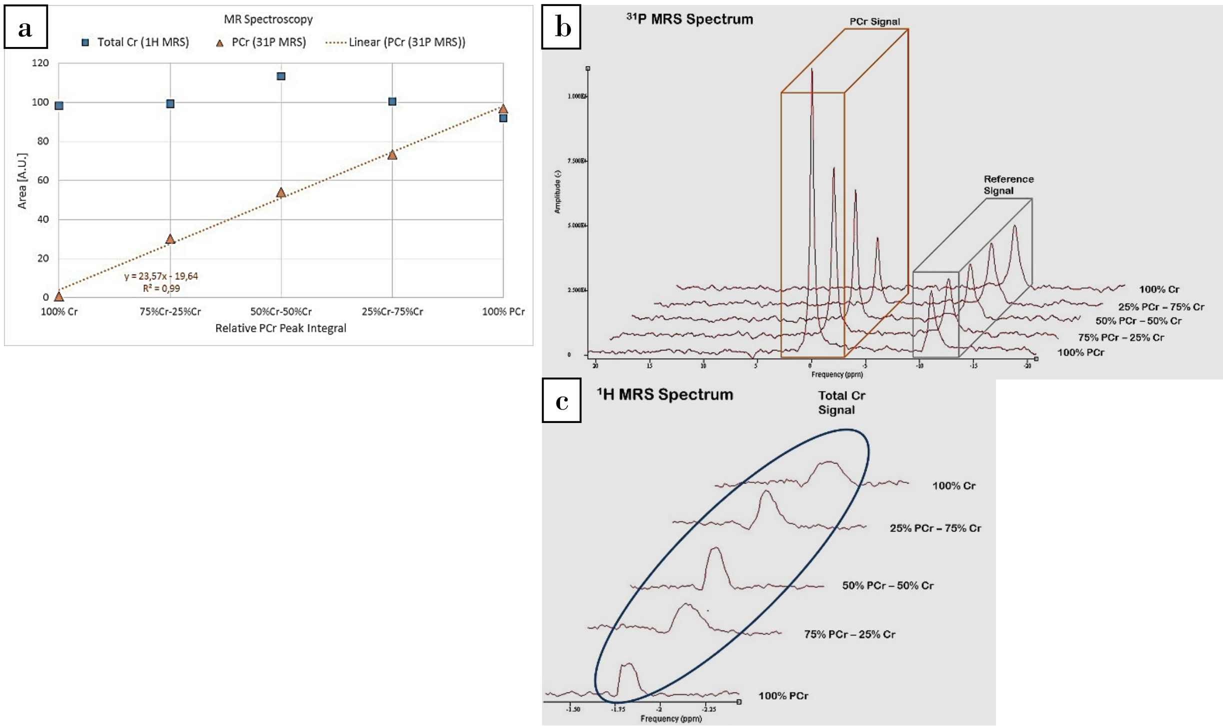

Fig. 5-12: ^{31}P-MRS and ^{1}H-MRS analysis for different concentrations between Cr and PCr.
(a) Comparison between PCr and total Cr evolution (areas under MRS spectra)
(b) ^{31}P-MRS spectra showing the peaks corresponding to PCr and a reference phantom
(c) ^{1}H-MRS spectra showing the peaks corresponding to total creatine (PCr + Cr)

5.3.2. pH contribution to CEST effect

The next experiment's results present the changing CEST effect with pH variations as it may occurs in muscle during exercise. *Fig. 5-13* and Fig. 5-14 shows an example of a Z-spectrum and CEST$_{asym}$ curves respectively for the samples described in 4.3.2:

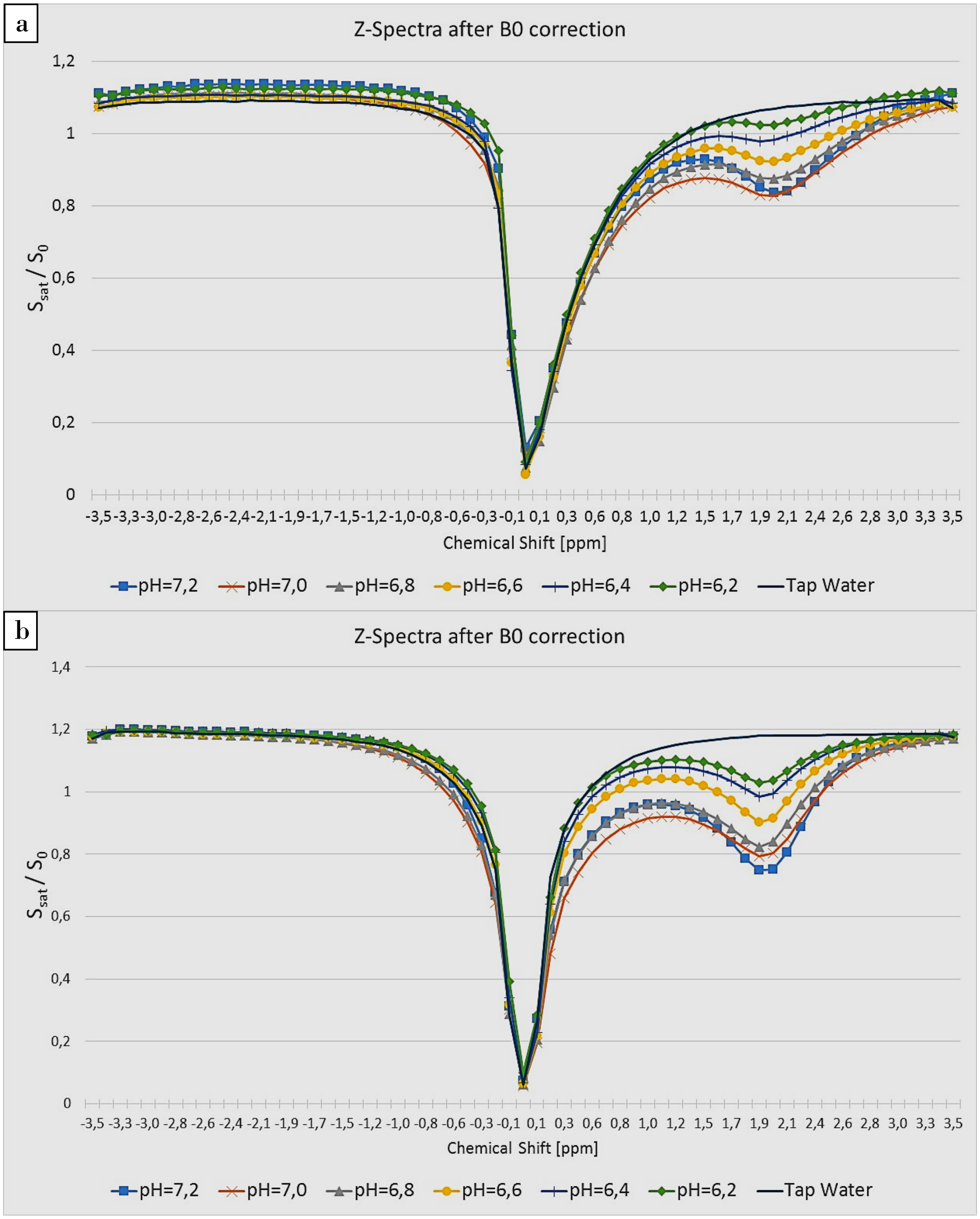

Fig. 5-13: Z-Spectra acquired with different readout modules. (B_1^+ Amplitude = 1.0 μT, 5 pulses of 100 ms)
(a) Readout module where all segments are read in 1 shot.- FA=1º
(b) Readout module where 2 segments are read per shot.- FA=5º

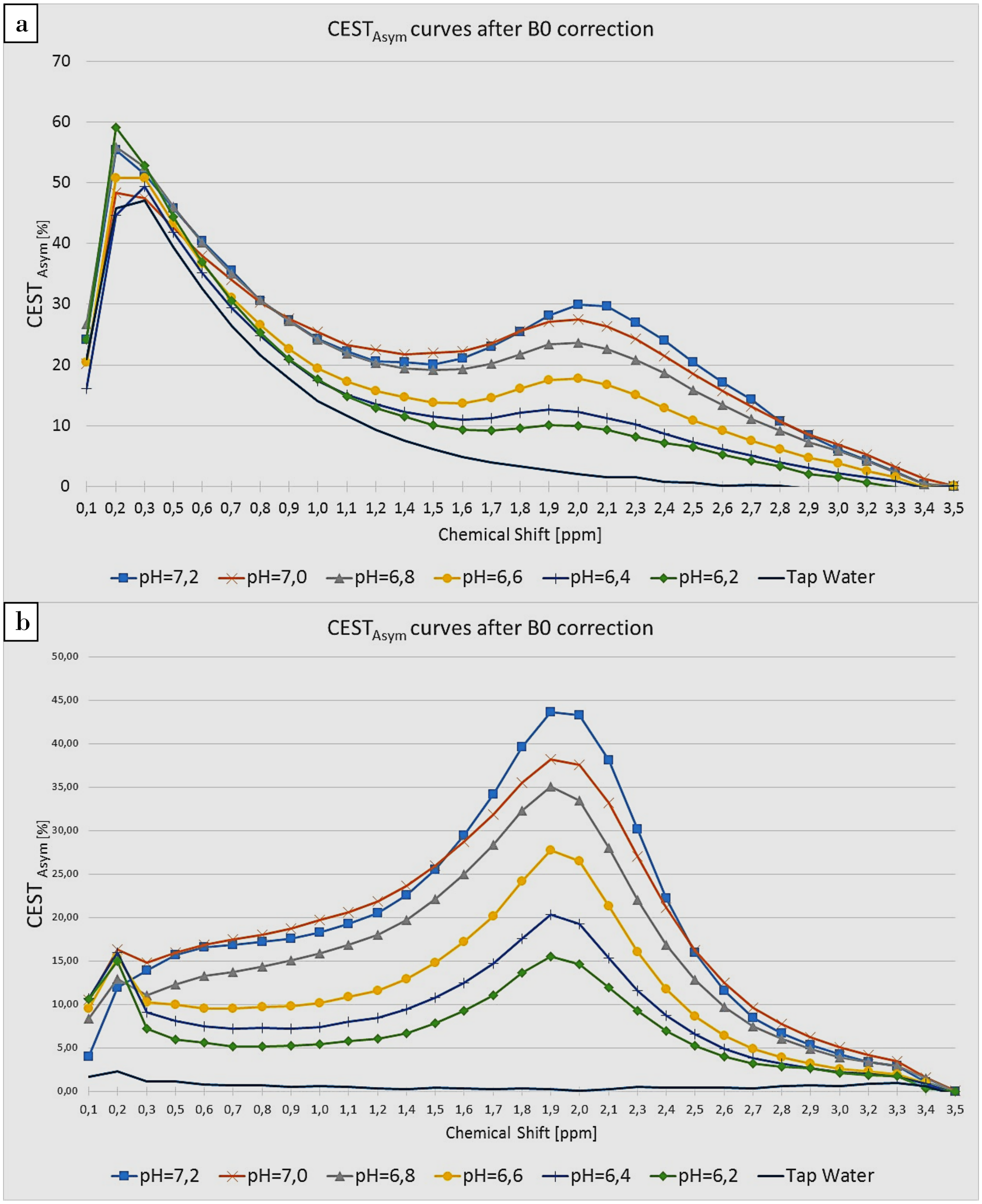

Fig. 5-14: CEST$_{Asym}$ curves for different readout modules. (B_1^+ Amplitude = 1.0 µT, 5 pulses of 100 ms)
(a) Readout module where all segments are read in 1 shot.- FA=1º
(b) Readout module where 2 segments are read per shot.- FA=5º

Fig. 5-15 shows as a summary, the contrast achieved by the solutions with different pH and how they are affected by four different B_1^+ amplitudes for the CEST saturation pulses, 0.7, 1.0, 1.5 and 3.8 µT. Linear regression lines and their formulas are also presented.

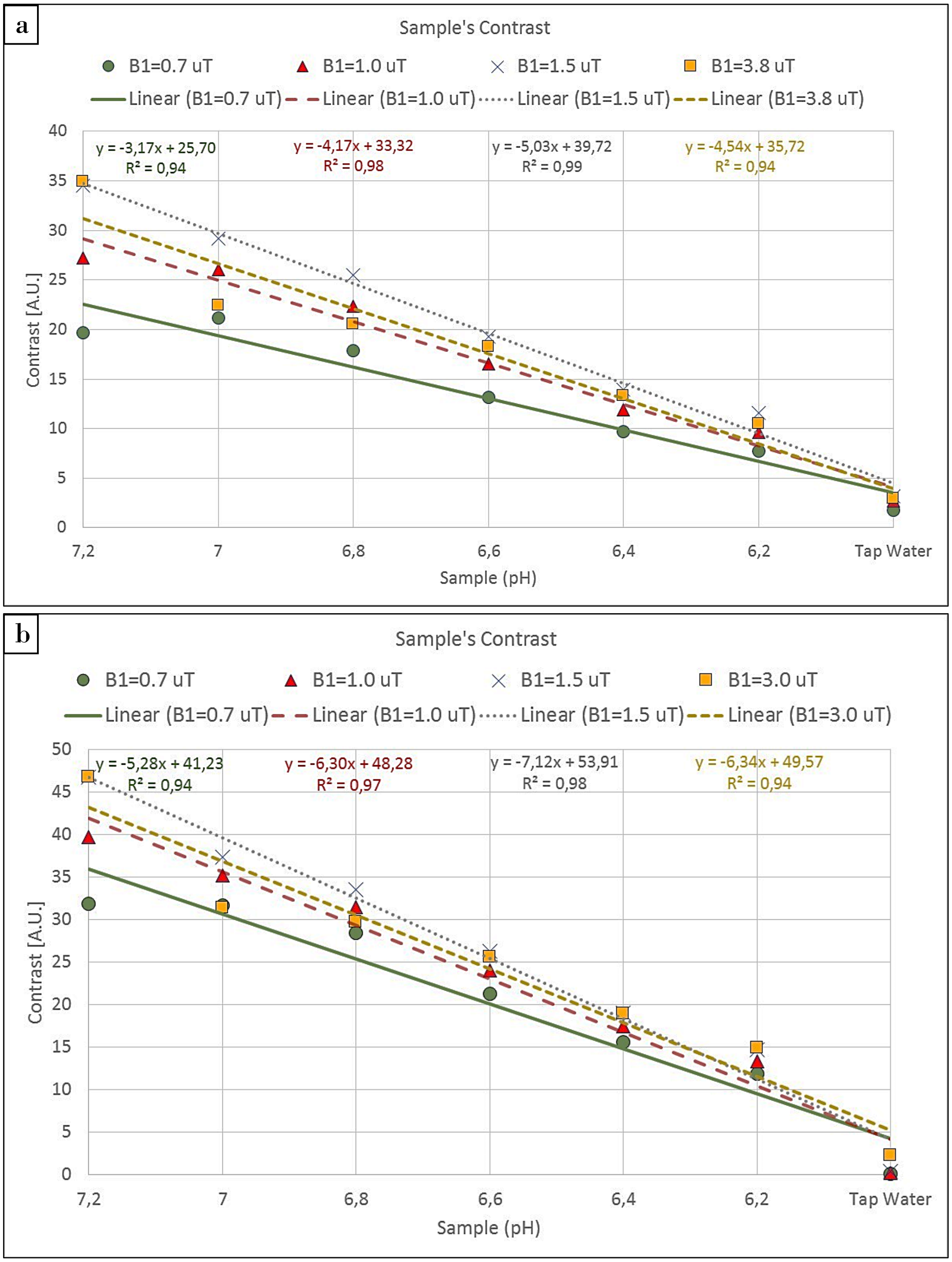

Fig. 5-15: Contrast achieved with different readout modules. (B_1^+ Amplitude vs. pH)
(a) Readout module where all segments are read in 1 shot.- FA=1°
(b) Readout module where 2 segments are read per shot.- FA=5°

Fig. 5-16 present the same data as in _Fig. 5-15_, but with B_1^+ amplitudes represented in the horizontal axis instead of pH.

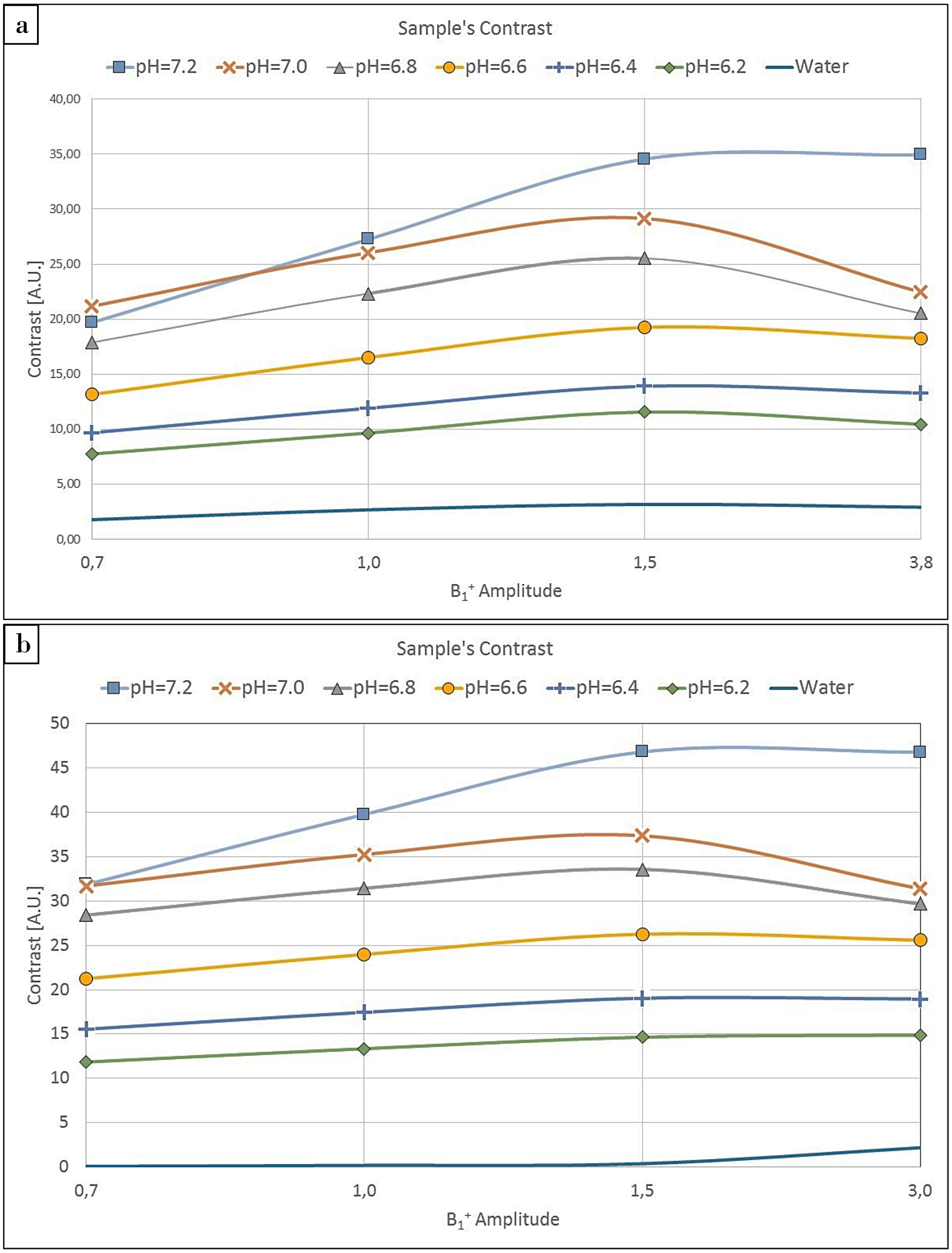

Fig. 5-16: Contrast achieved with different readout modules. (pH vs. B_1^+ Amplitude)
(a) Readout module where all segments are read in 1 shot.- FA=1°
(b) Readout module where 2 segments are read per shot.- FA=5°

The following results in *Fig. 5-17* show the effects of the excitation FA on the CEST contrast, as in 5.3.1, although for a lower range (1°, 2° and 3°); but in this case in relation with pH. The phase encoding reordering is also studied here. (Only for the readout module "all segments read in 1 shot" after the saturation B_1^+ is applied)

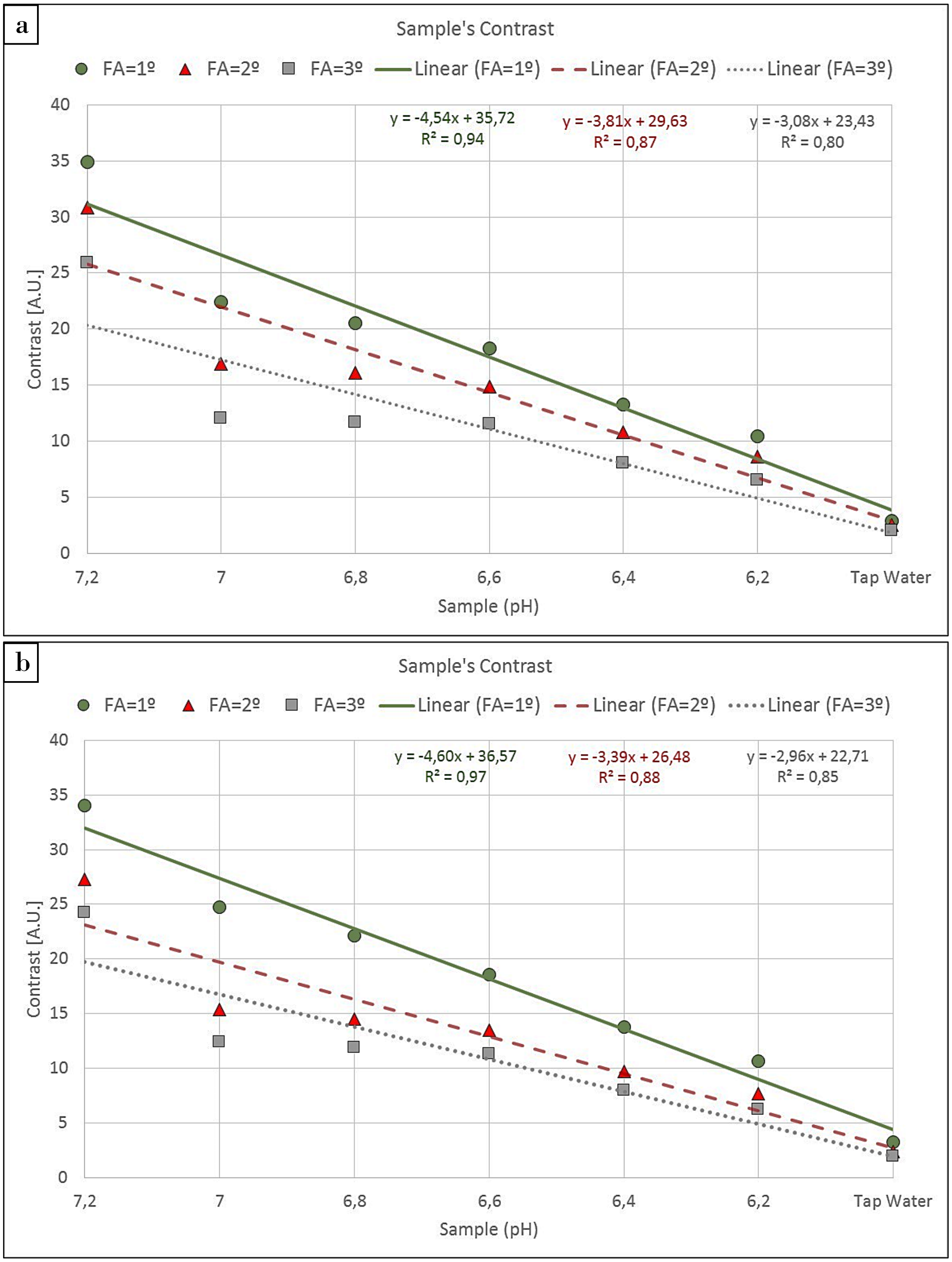

Fig. 5-17: Contrast achieved with different Phase encoding reordering. (FA vs. pH)
(a) Phase encoding reordering = Central.- All k-space segments read in 1 shot
(b) Phase encoding reordering = Linear.- All k-space segments read in 1 shot

The last results presented in *Fig. 5-18* show the effect of the phase encoding reordering as well as the offset distribution for a fixed flip angle (FA=1º). All k-space segments are acquired after the saturation pulses B_1^+ are applied.

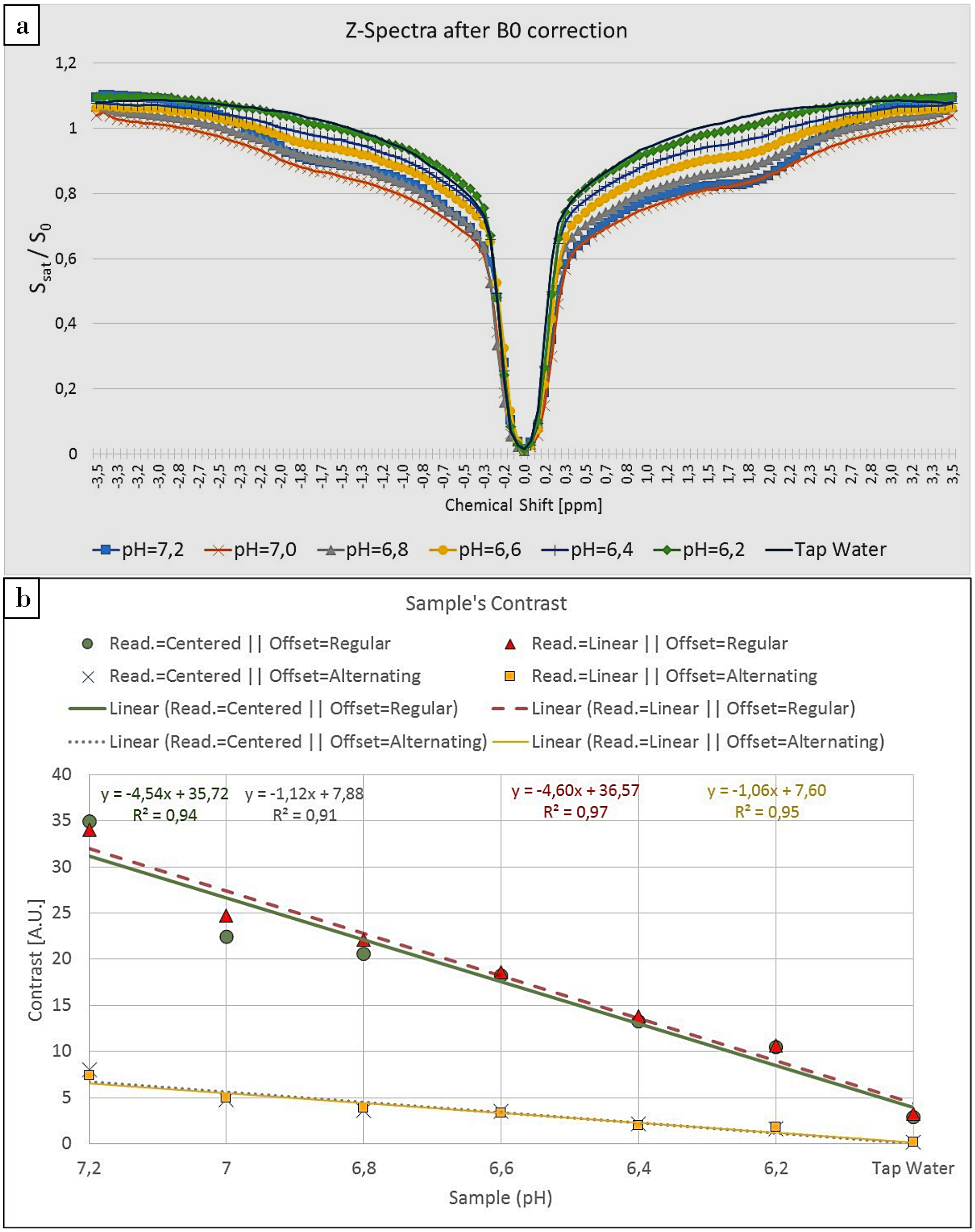

Fig. 5-18: Effect of Phase encoding reordering and Offsets distribution
(a) Z-Spectra acquired for different pH samples.- FA=1°, Offsets distribution = Alternating
(b) All 4 combinations of Phase encoding reordering and Offsets distribution

6. DISCUSSION AND CONCLUSIONS

This chapter's aim is to summarize the results presented after applying the tools and methods described previously, address the main challenges and possible future improvements towards a successful dynamic MR-based Cr-CEST study in vivo and finally provide an overview of the current thesis achievements.

6.1. Specificity of CEST contrast vs environmental factors in phantom study

From the environmental factors which influence the CEST effect, CK metabolites concentration and pH were selected to study their contributions.

6.1.1. CK metabolites concentration contribution to CEST effect

The main contribution to the image contrast is coming from free Cr, being between 3 to 5 times higher than the PCr, depending on the FA and readout module selected.

The relation between Cr concentrations and image contrast was linearly dependent with slopes between 6.36 and 7.22 (see figures presented in Section 5.3.1). This is translated into a gain of around 0.6 % in contrast per mMol of Cr in the solution.

6.1.2. pH contribution to CEST effect

pH has the effect of reducing the CEST effect for increasing acidic environments. This is the case also in muscle during exercise, however in the physiological range studied [6.2 -7.2], even at 6.2 some contrast was achieved.

In this range, the relation between pH and CEST contrast was found approximately linear with $R^2 > 0.94$ for FA=1°.

6.2. Specificity of Cr contrast vs MR sequence signal readout in phantom study

From the sequence parameters available by the user which influence the CEST mechanism and Image contrast, the following were selected:

6.2.1. Flip Angle (FA) of the excitation RF pulse

For in vitro measurements of solutions containing CK metabolites in PBS the optimum angle was found to be the minimum allowed by the software (minimum incremental of 1°).

When readout module "2 segments per shot" was selected, the FA in the range 1º-9º gave similar results, with high CEST image contrast achieved. On the contrary, it seems to be very sensitive to the FA when the readout module selected was "all segments per shot". See *Fig. 5-10.*

6.2.2. B1⁺ saturation pulse length and amplitude effect on CEST contrast

The B_1^+ saturation pulse length also influence the image contrast only when the module "all segments per shot" was selected. However these differences were not so pronounced compared to FA sensitivity. In this case the best results were achieved when the pulse length was the greatest tested (100 ms). See *Fig. 5-11.*

The B_1^+ saturation pulse amplitude was tested in solutions with different pH. Independently of the readout module selected. An amplitude of 1.5 µT was found optimum (*Fig. 5-16*). The effect of increasing amplitudes was the broadening of the CEST peaks.

6.2.3. Readout module contribution to CEST effect

When the readout corresponding to "2 segments per shot" was selected, the Z-spectrum was symmetric and the CEST asymmetry analysis was done according to the assumptions covered in Section 2.4 CEST Imaging.

This was not the case, when "all segments per shot" were set. The drawback of reading less number of segments after the saturation pulses were applied is that the total acquisition time increased dramatically (from around 2 min up to 22 min).

It looks like the asymmetry of the "all segments per shot" module was caused because there was not enough recovery towards equilibrium after the saturation at the previous Offset frequency. This is obvious in *Fig. 5-18.a*, where the Z-spectrum is symmetric but it looks like one side of the spectrum is influencing the other side due to the ***alternating*** Offsets distribution. This effect is seen as lowered values in the Z-spectra curve also for negative frequencies.

Nevertheless by applying certain saturation pulses, this readout module was given similar Cr-CEST contrast results. This is the case for FA=1º, for which the magnetization appears to have enough time to recover equilibrium before the next measurement takes place. This is patent in Fig. 5-9 and Fig. 5-10 for a FA=1º.

6.2.4. Phase encoding reordering contribution to CEST effect

Phase encoding reordering defined the order in which segments were measured in the k-space.

No remarkable differences were found between central and linear reordering, which means that the order at which the k-space lines are acquired in phase encoding direction during the readout period was not able to improve much the saturation contrast. See *Fig. 5-18*

6.2.5. Offsets distribution to CEST effect

Alternating acquisition of Offsets could be helpful to counteract moving artifacts during measurement. However, it has to be noted that the asymmetry observed for the readout "all segments per shot" was caused for insufficient recovery time between saturation periods. This has to be taken into consideration.

Fig. 5-18 shows how saturation effect leaks along the spectrum range, decreasing the CEST contrast around 80%.

6.3. Comparison between CEST analysis vs ^{1}H-MRS and ^{31}P-MRS

The results from the ^{1}H-MRS analysis shown in *Fig. 5-12* illustrate that the total Cr signal remains approximately constant independently if it is coming from PCr or free Cr. On the other hand, ^{31}P-MRS shows a high dependent linear relation (R^2=0.99) of PCr signal with its concentration within the solutions.

Cr-CEST imaging applied to the same metabolites concentrations show also a linear relation but with opposite sign. As expected, for increasing concentration of free Cr (like during exercise) the Cr-CEST signal is also increasing while PCr signal measured with ^{31}P-MRS is dropping.

6.4. Limitations

In order to perform a successful dynamic CEST study, a new sequence optimization will be required for in vivo measurements starting from the values found in the present work. Optimum FA is likely to change due to different physiological T_1 of tissue in vivo.

pH in vivo will not be controllable, mild exercise will be hence recommended unless pH can be measured dynamically in some other way (e.g., via ^{31}P-MRS).

Temporal resolution needs to be reduced for a dynamic CEST study, however too short gaps between acquisitions of different Offsets will cause inherently asymmetric Z-spectra, which will bias results. Some compensation has to be found to reach equilibrium between saturation periods.

6.5. Improvements

In order to increase temporal resolution, the following actions are suggested:

- ✓ Modifications in the spoil gradient pulses
- ✓ Placement of delays between saturation periods
- ✓ Different readout module with more efficient k-space acquisition

If measurements during exercise are required, motion correction algorithms will have to be implemented.

Besides the B_0 correction algorithm described, an additional one could also be implemented to overcome possible B_1 inhomogeneities.

6.6. Conclusions

As a first attempt, it has been proven that dynamic studies are possible with the current hardware and software available. After the listed limitations were overcome *Fig. 5-1 and Fig. 5-2* show how the compiled sequence was able to:

- ✓ Saturate the solute protons at up to 128 different frequencies
- ✓ Run the static sequence consecutively 60 times during 12 minutes

The results presented in Section 5.2.1 provide evidence for:

- ✓ The B_0 inhomogeneity was low enough for the water filled phantom to achieve a narrow water peak linewidth of less than 0.6 ppm
- ✓ Saturation was efficient, achieving a reduction of the H_2O signal greater than 96.5%

The modified Matlab processing tool is now able to reconstruct CEST images in a similar way as Siemens ICE does. The differences, depicted in *Fig. 5-4*, suggest:

- ✓ Remarkable differences for solid matter (plastic from bottle and syringes)
- ✓ Minor differences within the tap water fulfilling the phantom
- ✓ Negligible differences (and constant/stable) within the solutions inside the syringes

Fig. 5-6 and *Fig. 5-7* displayed that B_0 inhomogeneities were satisfactorily corrected and the integral ranges for $CEST_{asym}$ calculations were properly selected.

The presented work allows not only CEST data processing but also analysis, which provides a deeper understanding on how CEST contrast is affected by (i) environmental factors such as metabolites concentration and pH as well as (ii) by MR sequence parameters.

The presented MR sequence and image reconstruction is able to achieve a Cr contrast contribution greater than 80% when the readout module "all segments per shot" was selected. The other 20% is overlapped with the PCr contribution.

The same contribution was found after the readout module "2 segments per shot" was selected with an FA=1°. However further improvements are needed in this direction to increase temporal resolution due to asymmetric spectra.

Finally the following MR sequence parameters resulted in optimum detection of free Cr in phantoms for highest contrast:

- Spectrum range = ± 3.5 ppm
- Saturation pulses number and length = 5 pulses, 100 ms each
- FA= 1^o
- B_1^+ Amplitude = *1.5 μT*
- Offsets distribution = Regular
- Phase encoding reordering = Central
- Frequency shift = 1.9 ppm
- Delta frequency = 0.6 ppm

7. REFERENCES

1. Rabi, I.I., et al., *A New Method of Measuring Nuclear Magnetic Moment.* Physical Review, 1938. **53**(4): p. 318-318.

2. McRobbie, D.W., . and et al., *MRI from Picture to Proton*. 2006: Cambridge University Press.

3. van Zijl, P.C. and N.N. Yadav, *Chemical exchange saturation transfer (CEST): what is in a name and what isn't?* Magnetic Resonance in Medicine, 2011. **65**(4): p. 927-948.

4. Kogan, F., H. Hariharan, and R. Reddy, *Chemical Exchange Saturation Transfer (CEST) Imaging: Description of Technique and Potential Clinical Applications.* Curr Radiol Rep, 2013. **1**(2): p. 102-114.

5. Guivel-Scharen, V., et al., *Detection of proton chemical exchange between metabolites and water in biological tissues.* Journal of Magnetic Resonance, 1998. **133**(1): p. 36-45.

6. Dagher, A.P., et al., *Imaging of urea using chemical exchange-dependent saturation transfer at 1.5 T.* Journal of Magnetic Resonance Imaging, 2000. **12**(5): p. 745-748.

7. Haris, M., et al., *Exchange rates of creatine kinase metabolites: feasibility of imaging creatine by chemical exchange saturation transfer MRI.* NMR Biomed, 2012. **25**(11): p. 1305-1309.

8. Kogan, F., et al., *Method for high-resolution imaging of creatine in vivo using chemical exchange saturation transfer.* Magn Reson Med, 2014. **71**(1): p. 164-172.

9. Kogan, F., et al., *In vivo chemical exchange saturation transfer imaging of creatine (CrCEST) in skeletal muscle at 3T.* J Magn Reson Imaging, 2014. **40**(3): p. 596-602.

10. Haris, M., et al., *A technique for in vivo mapping of myocardial creatine kinase metabolism.* Nat Med, 2014. **20**(2): p. 209-214.

11. Schmitt, B., M. Brix, and S. Domayer, *CEST Imaging.* Current Radiology Reports, 2014. **2**(3).

12. Gadian, D.G., *NMR and its applications to living systems*. 1995, Oxford University Press. p. 29-33, 139-164, 171-174, 181-185.

13. Hanson, L.G., *Introduction to Magnetic Resonance Imaging Techniques.*, T.T. Groth, Editor. 2009: http://www.drcmr.dk/. p. 48.

14. Keeler, J., *Understanding NMR Spectroscopy*, in *Chapter 3:The vector model*. 2002, University of Cambridge: http://www-keeler.ch.cam.ac.uk/lectures/Irvine. p. 22.

15. Haacke, M., et al., *Magnetic Resonance Imaging: Physical Principles and Sequence Design*. 1999: Wiley-Liss.

16. JAMES, T.L., *Biophysics textbook online (Biophysical, Society)*. 2000, Biophysical Society: Bethesda, MD.

17. Freeman, R., *Magnetic Resonance in Chemistry and Medicine*. 2003, Oxford University Press. p. 26-29, 43-51, 223-239.

18. De Graaf, R.A., *In vivo NMR spectroscopy principles and techniques*. 2007, Hoboken, NJ: John Wiley & Sons.

19. Reusch, W. *Supplemental NMR Topics*. 2013 16/08/2015]; Available from: http://www2.chemistry.msu.edu/faculty/reusch/VirtTxtJml/Spectrpy/nmr/nmr2.htm#nmr11.

20. Reusch, W. *Nuclear Magnetic Resonance Spectroscopy*. 2013 16/08/2015]; Available from: http://www2.chemistry.msu.edu/faculty/reusch/VirtTxtJml/Spectrpy/nmr/nmr1.htm.

21. Zaiss, M. and P. Bachert, *Chemical exchange saturation transfer (CEST) and MR Z-spectroscopy in vivo: a review of theoretical approaches and methods.* Phys Med Biol, 2013. **58**(22): p. R221-269.

22. Zhou, J. and P.C.M.v. Zijl, *Chemical exchange saturation transfer imaging and spectroscopy.* Progress in Nuclear Magnetic Resonance Spectroscopy, 2006. **48**(2-3): p. 109-136.

23. Sedivy, P., et al., *Dynamic 31P MR spectroscopy of plantar flexion: influence of ergometer design, magnetic field strength (3 and 7 T), and RF-coil design.* Med Phys, 2015. **42**(4): p. 1678-1689.

24. Aime, S., et al., *Paramagnetic Lanthanide(III) complexes as pH-sensitive chemical exchange saturation transfer (CEST) contrast agents for MRI applications.* Magnetic Resonance in Medicine, 2002. **47**(4): p. 639-648.

25. Sun, P.Z., et al., *Investigation of optimizing and translating pH-sensitive pulsed-chemical exchange saturation transfer (CEST) imaging to a 3T clinical scanner.* Magn Reson Med, 2008. **60**(4): p. 834-841.

26. Haase, A., et al., *FLASH imaging: rapid NMR imaging using low flip-angle pulses. 1986.* J Magn Reson, 2011. **213**(2): p. 533-541.